UC Irvine
UC Irvine Electronic Theses and Dissertations

Title
Soft Robotic Actuators

Permalink
https://escholarship.org/uc/item/1wc522f5

Author
Godfrey, Juleon Taylor

Publication Date
2017

Peer reviewed|Thesis/dissertation

eScholarship.org Powered by the California Digital Library
University of California

UNIVERSITY OF CALIFORNIA,
IRVINE

Soft Robotic Actuators

THESIS

Submitted in partial satisfaction of the requirements
for the degree of

MASTER OF SCIENCE

In Mechanical and Aerospace Engineering

By

Juleon Taylor Godfrey

Thesis Committee:
Professor Gregory Washington Irvine, Chair
Professor Faryar Jabbari
Professor David Reinkensmeyer

2017

© 2017 Juleon Taylor Godfrey

Table of Contents

List of Figures

List of Tables

Acknowledgements

I would like to thank my adviser Dr. Greg Washington for his leadership and guidance over the years as an undergraduate and graduate student. If it weren't for his encouragement I wouldn't have gone to graduate school to pursue an MS degree.

I would like to thank Robin Jeffers for her years of support and counseling through my undergraduate degree. She always made sure I was heading in the right direction in order to complete my degree.

I would like thank my fellow ISSL lab members for making my time at UCI a lot more enjoyable. This group of people has made UCI a much better place to be at. Especially Joseph Bell, Vatche Donikian, Kyle Van Volkinburg, Summer Dumas, Joseph Garcia, and Theron Smith for helping setup experiments, test equipment, and ordering countless parts for my projects.

Finally, I would like to thank my family and friends who have provided me a strong foundation which I could be build my career and dreams. Especially, my parents Julie and Leo and dog Roxy for always supporting my academic career. Without the help of all these people this publication would not have been possible.

Abstract

Soft Robotic Actuators

By

Juleon Taylor Godfrey

Master of Science in Mechanical and Aerospace Engineering

University of California, Irvine, 2017

Dean Gregory N. Washington Irvine, Chair

In this thesis a survey on soft robotic actuators is conducted. The actuators are classified into three main categories: Pneumatic Artificial Muscles (PAM), Electronic Electroactive Polymers (Electric EAP), and Ionic Electroactive Polymers (Ionic EAP). Soft robots can have many degrees and are more compliant than hard robots. This makes them suitable for applications that are difficult for hard robots. For each actuator background history, build materials, how they operate, and modeling are presented. Multiple actuators in each class are reviewed highlighting both their use and their mathematical formulation. In addition to the survey the McKibben actuator was chosen for fabrication and in-depth experimental analysis. Four McKibben actuators were fabricated using mesh sleeve, barbed hose fittings, and different elastic bladders. All were actuated using compressed air. Tensile tests were performed for each actuator to measure the tension force as air pressure increased from 20 to 100 psi in 10 psi increments. To account for material relaxation properties eleven trials for each actuator were run for 2-3 days. In conclusion, the smallest outer diameter elastic bladder was capable of producing the highest force due to the larger gap between the bladder and the sleeve.

Introduction

Soft robotics focuses on using soft, flexible materials for robotics applications, instead of rigid hard joints used for typical robots. Soft materials allow for increased degrees of freedom. Soft robotics have many applications including biorobotic, medical, industrial, and aerospace [1], [2]. The main goal of soft robotics is to create robots that are compliant and mimic natural movement. Soft robots can also be referred to as artificial muscles because they have characteristics identical to biological muscle.

This thesis will focus on two branches of soft robotics: Pneumatic Artificial Muscles (PAMs) and Electroactive Polymers (EAPs). PAMs utilize a fluid, mostly air, to generate a force due to a change in the actuators internal pressure. PAMs convert fluid energy into mechanical energy usually in the form of linear displacements. The history of PAMs can be traced back to the 1950s with A.H. Morin's patent for an elastic diaphragm. EAPs can be classified into two categories electric and ionic. Electric EAPs require an electric field to activate the actuator and ionic EAPs require electrolyte and an electric field to actuate. EAPs history can be traced back to the 1800s with Henry Letheby's discovery of conductive polymers, Wilhelm Conrad Roentgen discovery of dielectric elastomer, and Pierre and Paul-Jacques Curie's discovery of piezo electricity. Even though soft robots have been around for a long time a recent resurgence in research is taking place due to advancements in robotics and biological inspiration. Researchers have used soft robots to produce the natural movement of animals that hard robots can't mimic.

In chapter 5 a representative actuator was chosen and constructed for tensile testing. The McKibben actuator was chosen as representative actuator due to the extensive research done on this actuator. The McKibben actuator is capable of replicating movements similar to natural

muscle making it suitable for many applications. Finally, concluding remarks and future work are discussed about soft robotics. Suggestions are also made about the future research needed in soft robotics.

Chapter 1: What Are Soft Robotics

Soft robotics is the branch of robotics that focuses on use of soft, flexible components instead of rigid, solid joints that traditional robots utilize. In addition to using soft, compliant components, soft robots are actuated using a fluid (liquid or pneumatic) or electricity. Pneumatic artificial muscles (PAMs) and Electroactive polymers (EAPs) are the two main types of soft robots. There are two types of EAPs: electronic and ionic. Electronic EAPs use electricity as their actuation method and ionic EAPs use mobile ions as an actuation method.

Some of the advantages of soft robots are there ability to reproduce more complex movements, emanating from the fact that they are light weight, and flexible. Unlike hard robots made of rigid components soft robots use lighter and more flexible materials that can conform and bend to produce more natural movement.

Some of the main disadvantages of soft robotics are difficulty modeling and limited effectiveness compared to hard robots. Modeling these robots is difficult due to the many degrees of freedom for movement meaning conventional hard robotic approaches are hard to apply to soft robots. Another challenge for soft robotics is fabrication. Fabricating soft robots are more difficult than hard robots due to more complex building procedures and the unique build materials. Due to these disadvantages, replacing hard robots with soft robots would be a difficult.

Chapter 2: Pneumatic Artificial Muscles (PAMs)

2.1 Morin Muscle

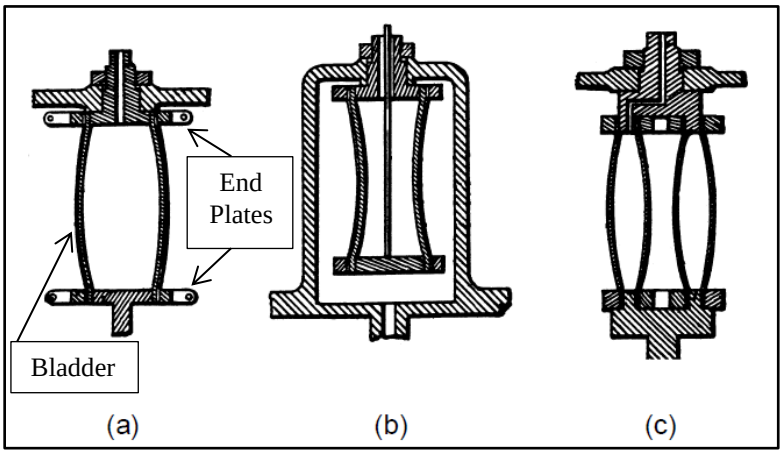

Figure 1:Image of Morin Muscles [3]

The Morin muscle was created in 1953 by Alexandre Henri Morin [4]. This muscle consists of an elastic bladder, with embedded fibers, that expands when inflated causing the muscle to contract. Figure 1 shows Morin's design for three different versions of his elastic diaphragm: an overpressure design (a), an under-pressure design (b), and a concentric membranes design (c). A fluid fills the diaphragm and expands circumferentially outward while the actuator contracts longitudinally. Morin deigned the diaphragm to be a replacement for a piston or spring, in which position and spring constant could be changed by altering the internal pressure of the diaphragm. The overpressure design works by the elastic diaphragm diameter increasing which causes the actuator to shorten, as internal pressure increases. The underpressure design works by increasing the pressure in the outer chamber, causing the internal diaphragm to contract. When the internal pressure of the concentric design is increased, the outer diaphragms diameter increases while the inner elastic diaphragms diameter decreases. In the patent Morin suggested the diaphragm be

made from rubber and the fiber reinforcement could be made of thread. This actuator force is limited by the strength of the thread adding addition threads can increase the force of the actuator. The threads prevent damage to the bladder as the internal air pressure is increased. Many of the pneumatic muscles in this section were derived from the Morin's patent of the elastic diaphragm.

2.2 McKibben Actuator

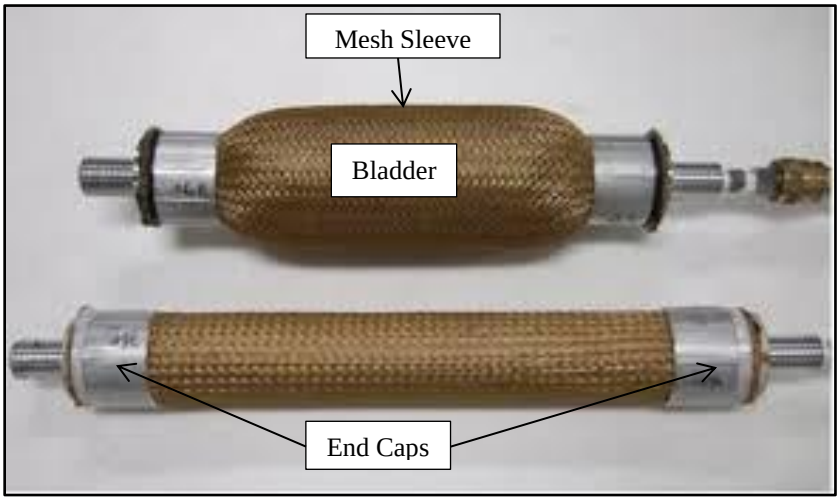

Figure 2: Image of McKibben actuator

The McKibben actuator was created by Joseph L. McKibben in the 1950s based of a patent by A.H. Morin [3] . McKibben actuators consist of an internal bladder and external mesh sleeve. As the internal air pressure of the bladder is increased the bladder expands radially outward while the entire actuator contracts. Figure 2 shows a McKibben actuator at rest (bottom) and contracted (top). The McKibben muscle is also known as the fluidic muscle or actuator. The sleeve provides strength for the actuator by preventing damage to the elastic bladder. A McKibben actuator is fabricated using an elastomeric expandable tube or bladder, an expandable mesh sleeve, and clamps or ties to hold the actuator together. Even though the McKibben actuator is linear in

motion, multiple actuators can be connected to create bending motion. Placing two McKibben actuators in an antagonistic setup can create a rotating motion when the pressure in one of the McKibben actuators increases. Section 1.12 discusses an actuator consisting of segments made from multiple McKibben actuators.

2.2.1 McKibben Actuator Model

$$F(\theta, P) = \frac{\pi D^2 P}{4}(3\cos^2\theta - 1) \tag{2.1}$$

$$D = \frac{b}{n\pi} \tag{2.2}$$

$$V = \frac{1}{4}\pi D^2 L \tag{2.3}$$

$$V = \frac{1}{4}\pi (D - 2t_k)^2 L \tag{2.4}$$

$$F = \frac{\pi D^2 P}{4}(3\cos^2\theta - 1) + \pi P\left[Dt_k\left(2\sin\theta - \frac{1}{\sin\theta}\right) - t_k^2 \right] \tag{2.5}$$

$$F = \frac{\pi D^2 P}{4}(3\cos^2\theta - 1) + \pi D k_e\left[L\sin\theta - \frac{\pi\cos^2\theta}{\sin\theta}(D\sin\theta - d_0) \right] - \pi LDP_c(u_s + u_{st})\sin\theta \tag{2.6}$$

$$P_c = P - P_i \tag{2.7}$$

The model was developed by Ching-Ping Chou and Blake Hannaford [5]. Equation (2.1) represents the force (F) of the actuator as a function the diameter (D), the internal pressure (P), and the fiber angle with respect to the longitudinal axis (θ). Equation (2.1) neglects the thickness

of the elastic bladder (t_k). Equation (2.2) relates the diameter, when θ=90°, to the length of thread (b) and the number of times wrapped around the actuator (n).

For most fiber reinforced pneumatic artificial muscles (PAMs) fiber angle is important for determining the characteristics of an actuator. Equations (2.3) and (2.4) are the volume of the actuator, (2.3) neglects the wall and (2.4) accounts for wall thickness. Equation (2.5) is similar to (2.1) but accounts for the thickness of the elastic bladder. Equation (2.6) is the original equation for the tension force of a McKibben actuator by Hal F. Schulte Jr. This equation takes into account the length of the actuator (L) and the elastic constant of the internal tubing (k_e) [6]. (P_i) is the pressure required to inflate the tube without the sleeve to equal the diameter of the sleeved actuator. The difference between this pressure and the sleeved actuator is variable (P_c). This equation also accounts for two sources of friction: the coefficient between the threads in the sleeve (u_s) and the coefficient between the sleeve and the elastic tube (u_{st}). Equations (2.1) and (2.5) were simplified models developed by C. Chou and B. Hannaford.

$$F\left(\varepsilon,P\right)=\left(\pi r_0^2\right)P\left[a_c\left(1-k\varepsilon\right)^2-b_c\right] \tag{2.8}$$

$$\varepsilon=\frac{\left(l_0-l\right)}{l_0} \tag{2.9}$$

$$a_c=\frac{3}{\tan^2\left(\alpha_0\right)} \tag{2.10}$$

$$b_c=\frac{1}{\sin^2\left(\alpha_0\right)} \tag{2.11}$$

$$k=a_k e^{-P}+b_k \tag{2.12}$$

$$\varepsilon_{\max} = \left(\frac{1}{k}\right)\left(1-\sqrt{\frac{b}{a}}\right) \tag{2.13}$$

Another model was developed by B. Tondu and P. Lopez [7]. Equation (2.8) is the exerted force as a function of contraction, internal air pressure, and the initial radius of the internal bladder. The variables (a_c) and (b_c) depend on the angle between the longitudinal axis and the mesh sleeve (α_0). To account for the deviation of the cylinder shape due to the end connectors a factor (k) is multiplied to the contraction. There are two ways to find this factor: Through experimentation or using equation (2.12) where variable (P) is the internal air pressure. Using the equation (2.13) the maximum contraction of the actuator can be found. These equations are useful because they make a relation between the length of the actuator and the exerted force.

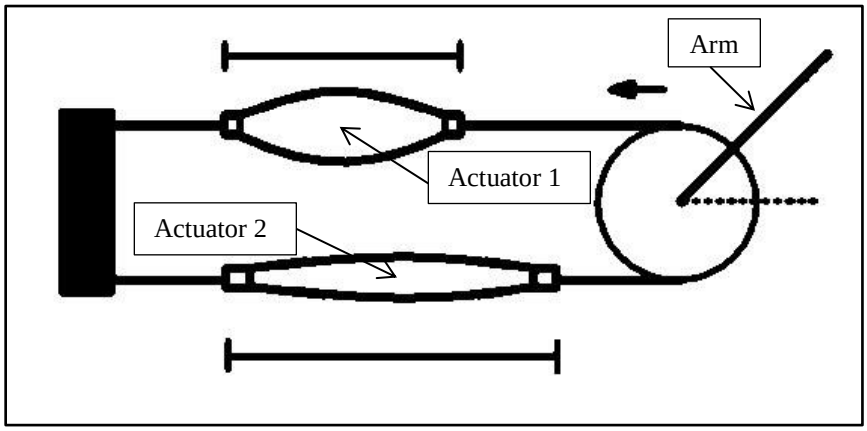

Figure 3: Image of McKibben actuator antagonistic setup

$$T = R\left[F_1\left(\varepsilon_1, P_1\right) - F_2\left(\varepsilon_2, P_2\right)\right] \tag{2.14}$$

$$\varepsilon_1 = \varepsilon_0 + \frac{R\theta}{l_0} \tag{2.15}$$

$$\varepsilon_2 = \varepsilon_0 - \frac{R\theta}{l_0} \tag{2.16}$$

One unique feature of the McKibben actuator is the ability of two actuators to be used in an antagonistic setup. Figure 3 is the image of two McKibben actuators in an antagonistic setup. In this figure actuator 1 is compressed (increased internal air pressure) while actuator 2 elongates (at rest or lower internal air pressure than actuator 1) causing the arm to move up. This setup can also be applied to other PAMs to create rotational movements. Equation (2.14) is the torque output when two McKibben actuators are placed in an antagonistic setup. The subscript 1 and 2 denote the properties of each actuator. Variable (R) is the radius of the wheel or sprocket that that changes the actuators change of pressure into rotational angle (θ). This ability with PAMs makes them more suitable for many applications.

2.3 Bellows Actuator

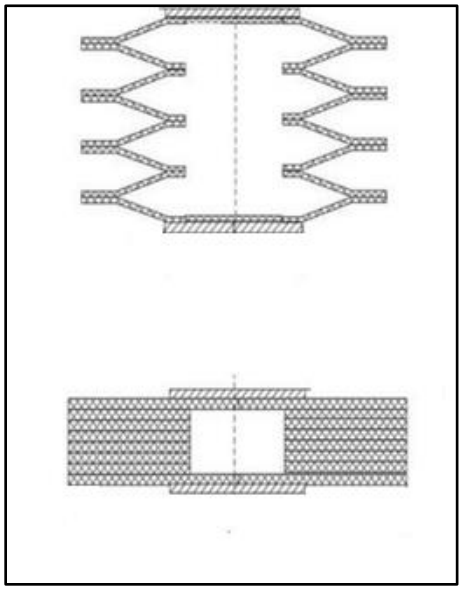

Figure 4: Image of Bellow Actuator

The Bellows actuator was created by D. C. Pridham Jr. in 1967 [8]. The bellow actuator has an elastomeric bladder that contains pleats that run perpendicular to the longitudinal axis. Pridham's patent suggests the bladder be constructed from polypropylene. When actuated the overall diameter reduces while the length of the actuator increases. Figure 4 is an example of the diameter change a bellow actuator experiences as internal air pressure is increased. This actuator bellows have a circular shape, but other cross section shapes can be utilized for this actuator such as square or star shaped bellows. Circular cross-sections can withstand greater forces but have restricted elongation, but square cross-sections experience greater deformation than circular cross-sections.

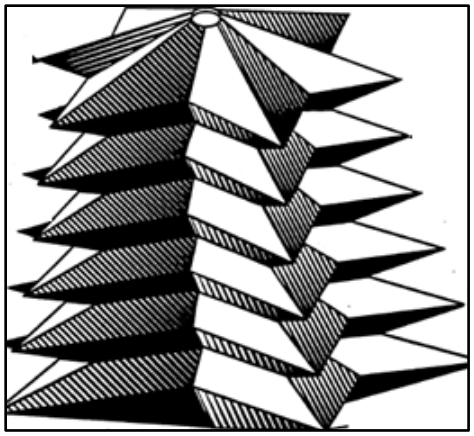

Figure 5: Image of Star shaped bellow actuator [9]

In 1993 Guy Immega created an improved design to the bellow actuator. Instead of the common circular shaped bellows, a star shaped bellow was utilized[9]. The star shaped bellows reduced overall shear stress compared to circular bellows. Reduced shear stress on the bellows results in greater elongation over the circular bellow actuators. Figure 5 is an image of the star shaped bellow actuator. Immega also observed the increasing the number of points of the star. He found that increasing the number of points on the star meant the ratio of short fold line (distance from

the center to the intersecting edges) to the long fold line (distance from the center to the corner vertices) had to be increased in order to obtain optimal performance from the actuator. Three is the minimum number of points needed for the star shaped actuator.

2.3.1 Bellow Actuator Model

$$F_a = -P\frac{dV}{dL} \tag{2.17}$$

The equation was used by Immega to describe the bellows actuator [9]. Equation (2.17) represents the force of the actuator (F_a) as a function of internal pressure (P), the change in volume (dV), and the change in the length (dL). Equation (2.17) is negative because as the actuator is elongated the force exerted decreases. Bellow actuators exert a greater force for shorter elongations than for longer elongations.

2.4 Yarlott Muscle

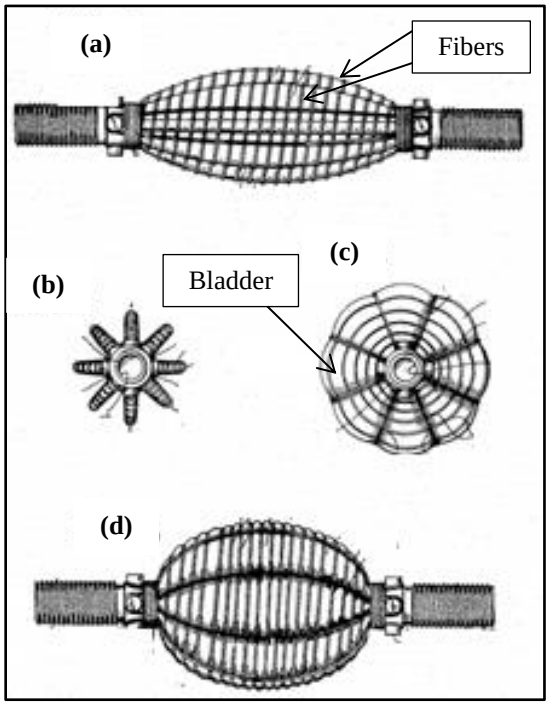

Figure 6: Image of Yarlott muscle [10]

The Yarlott was created by John M. Yarlott in 1972 [10]. This muscle consists of prolate spheroid shaped bladder with fiber reinforcement that is wrapped helically around the bladder. This actuator has one strand that is wrapped around the entire length of the elastic bladder. Figure 6 has images has two different views of an unactuated (a, b) and actuated (c, d) Yarlott muscle. When the actuator is at rest the bladder has pleats parallel to the longitudinal axis that unfolds when the pressure inside the actuator is increased. When actuated the actuators surface area remain constant meaning greater conversion of fluid energy to mechanical energy. This also means the actuator can be used with pressures as low as 0.25 psi. In the patent Yarlott suggest the bladder be made from neoprene and strong strand that can resist the elongation of the actuator.

2.5 Robotic Muscle Actuator (ROMAC)

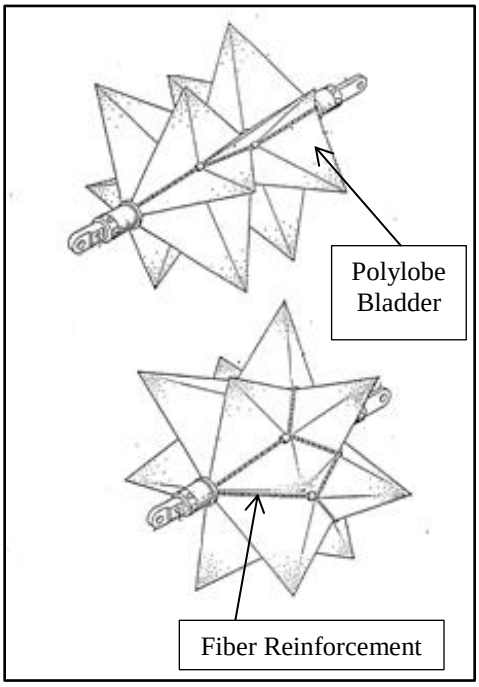

Figure 7: Image of ROMAC Actuator [11]

The RObotic Muscle Actuator (ROMAC) was created by Guy Immega and Mirko Kukolj in 1986 [3]. This actuator is made of a wire scaffold that holds up a polylobe bladder and a second set of fiber on the outside of the bladder. When internal air pressure is increased the actuator expands radially outward while the actuator contracts axially. If the internal pressure within the actuator is decreased the actuator contracts circumferentially and the actuator elongates along its longitudinal axis. Figure 7 shows a ROMAC at rest (top) and pressurized (bottom). For this actuator the bladder has to be stronger and stiffer than the other PAMs due to the added friction from the internal scaffolding that could be a source of actuator failure. The patent for this actuator sites rubber or plastic with nylon or Kevlar reinforcement as a suitable membrane. Elastic materials for bladder allow forces to be evenly distributed around the actuator, but non-elastic material could also be used to avoid failures in the bladder. The interior scaffolding has to

be strands that are strong and inextensible, such as, steel cables, joined twine, and synthetic fibers. If the Romac actuator is small or used at low pressure then the interior scaffolding is not required and the tension can be supported by only the bladder.

2.5.1 ROMAC Actuator Model

$$P = \frac{2T}{R} \tag{2.18}$$

$$F = 2T\cos(b) \tag{2.19}$$

$$F_F = \frac{Fl}{M\sin(c)} \tag{2.20}$$

$$F_a = NF_f\cos(d) = -P\frac{dV}{dL} \tag{2.21}$$

Equation (2.18) relates the internal pressure (P) of the actuator to the actuators radius of curvature (R) and the tension force per fabric unit width (T). Equation (2.19) shows the relation between the perpendicular force on the cable segment (F) and the half angle between force (F) and thread (b). Equation (2.20) relates the adjacent cable segment tension (F_F) to the number of connecting segments (M), the length of the segment (l), and the angle between two adjacent cable segments (c). Equation (2.21) gives the actuator force (Fa) as a function of the adjacent cable segment tension, the number of cable segments (N), and the angle between the longitudinal axis and the cable segment (d).

2.6 Paynter Knitted Muscle

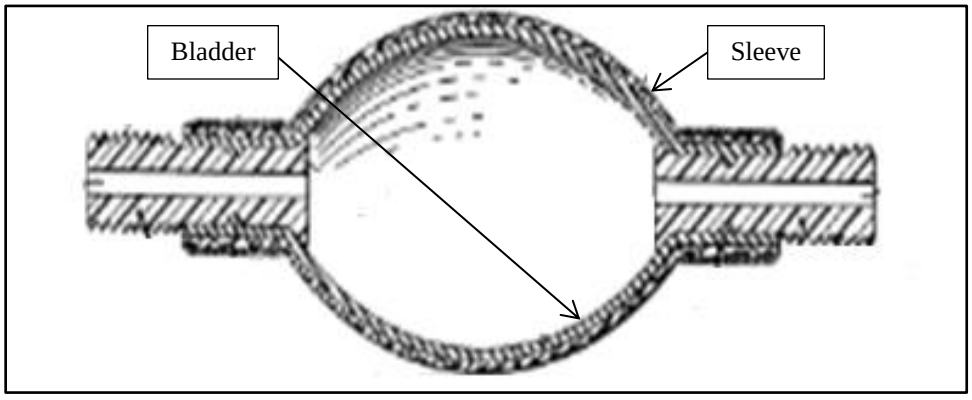

Figure 8: Image of Paynter knitted muscle [12]

This actuator was created by Henry M. Paynter in 1988 [12]. This actuator contains a spherical shaped bladder with a flexible fiber reinforced sleeve cover. Figure 8 is an image of the Paynter knitted muscle actuator. When this actuator is inflated it contracts, but when under negative pressure this actuator extends in length. This actuator was design to work at pressures greater than 29 psi. The bladder should be made out of an elastomeric material such as neoprene and the fiber reinforcements should be made from synthetic yarn. A bonding agent containing latex, silicon, or neoprene rubber is used to bond the fiber sleeve to the elastic bladder. Paytner suggest the sleeve be placed around the inflated bladder then the cover with bonding agent, then the actuator is dried using hot air, and finally the actuator is reinflated inside a mold and left to cure in order to give the actuator its spherical shape. To cure the actuator, while inside the mold, the actuator is placed in an oven.

2.7 Paynter Hyperboloid Muscle

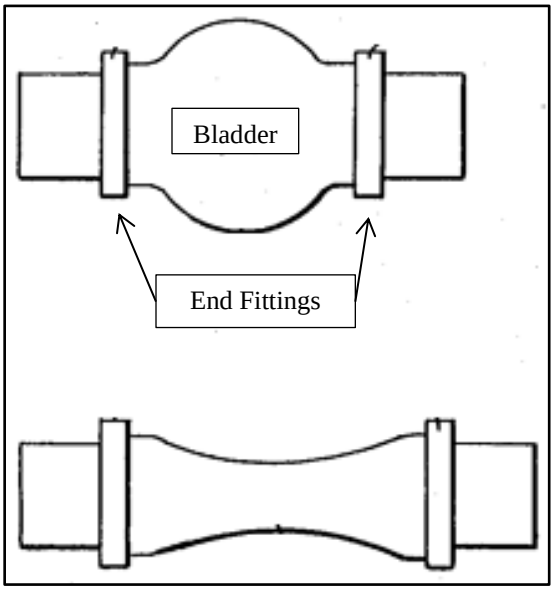

Figure 9: Image of Hyperboloid muscle [13]

Similar to the Paynter Knitted Muscle the Paynter Hyperboloid muscle was created by Henry M. Paynter in 1988 [13]. This actuator has a hyperboloid shaped bladder with fiber reinforcement. When the internal pressure is increased the muscle expands radially and contracts in length; at rest the muscle contacts radially and elongates along the longitudinal axis. When contracted the muscle has a spherical shape and when extended (at rest) the actuator has a hyperboloid shape. Figure 9 is an image of a contracted muscle (top) and an extended muscle (bottom). Paynter suggests the bladder be made from neoprene or polyurethane and the fiber reinforcement has to be flexible and inextensible such as Dacron or Kevlar. Paynter suggests that at gauge pressures less than 15 psi fiber reinforcement is not needed but at gauge pressures up to 125 psi fiber reinforcement is needed. The angular rotation difference between the two ends is known as the pitch angle. When the actuator is pressurized the fibers become parallel with the longitudinal axis creating a pitch angle of 0 degrees.

2.7.1 Paynter Hyperboloid Muscle Model

$$A(x) = \frac{F(x)}{P} = width \bullet depth \tag{2.22}$$

$$V(x) = \int_0^x A(x)dx = \sum_0^x A(x)\Delta x \tag{2.23}$$

$$dV(x) = A(x)dx \tag{2.24}$$

$$F(x) = P(x)\frac{dV(x)}{dx} \tag{2.25}$$

$$\theta_{Pitch} = \frac{360°}{n} \tag{2.26}$$

The model is from the hyperboloid patent by Paynter. V(x) and A(x) are the respective volume and area at a certain position (x). The area can be found from either multiplying the width and depth of the actuator, or dividing the generated force (F(x)) by the gauge pressure (P). Equation (2.24) is the governing force equation for the hyperboloid muscle. The pitch angle is found by dividing 360 degrees by the number of stands (n).

2.8 Kukolj Muscle

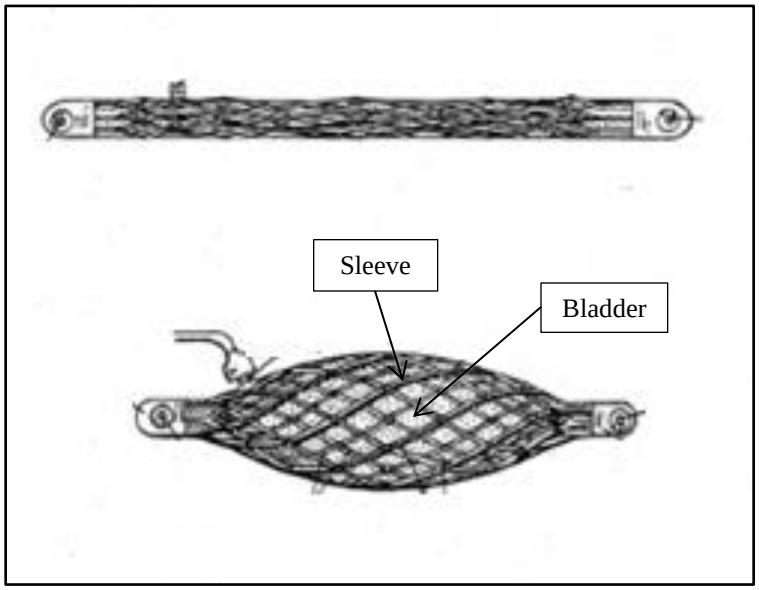

Figure 10: Image of Kukolj muscle [14]

The Kukolj Muscle was discovered by Mirko Kukolj in 1988 [14]. This actuator is similar to the McKibben actuator with the exception the mesh sleeve is replaced by a more open mesh net. At rest the actuators sleeve has a prolate shape around the bladder, wider diameter at the center and smaller diameter at the ends. When the actuator is extended the sleeve diameter becomes constant, conforming to the bladder. When actuated this inflated it contracts axially while expanding circumferentially outward. An actuated Kukolj muscle (bottom) and an unpressurized Kukolj muscle (top) is shown in Figure 10. Kukolj suggest the bladder be made of elastomeric material, like rubber or elastomeric plastic, and inextensible, flexible fiber such as plastic covered braided wire. Kukolj suggest placing a layer of oil, grease, or petroleum jelly in between the sleeve and bladder to reduce friction.

2.8.1 Kukolj Muscle Model

$$F = \int_S \frac{Pds}{\sin(a)} \tag{2.27}$$

$$|FL1| = |FT2| = \frac{|FL/2|}{\sin a} \tag{2.28}$$

$$|FT| = |FT1| + |FT2| = \frac{|FL|}{\sin a} \tag{2.29}$$

$$D = L - L\cos a \tag{2.30}$$

The equations above are from the patent for the Kukolj Muscle [14]. Equation (2.27) relates the pulling force (F) of the actuator to the internal pressure (P) and the angle (a) is between the longitudinal axis and a line tangent to the surface. This equation is integrated over the surface area (S). A perpendicular force applied to the center of a strand is equivalent to an expanding bladder. In equations (2.28)-(2.30), the variable (FL) is the perpendicular force, (FT) is the tension force, (a) is the angle between the longitudinal axis and the strand, (L) is the length of the bladder, and (D) is the distance the load moved.

2.9 Flexible Microactuator (FMA)

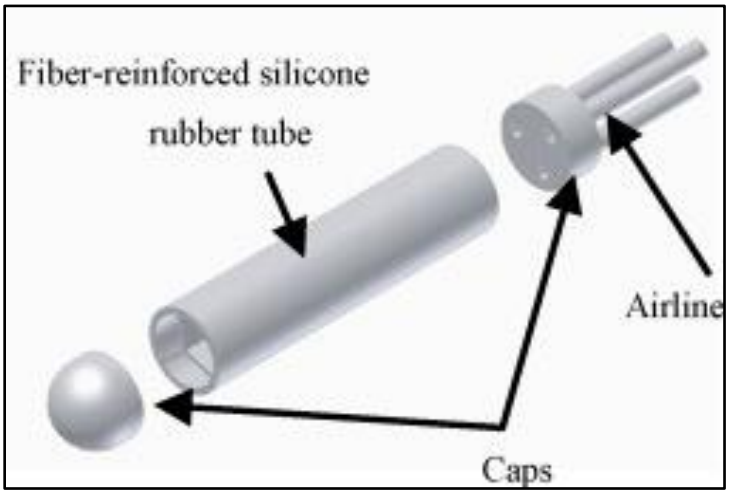

Figure 11: Image of Flexible Microactuators (FMAs)

The flexible microactuator (FMA) was created by Koichi Suzumori in 1989 [15]. This actuator consists of elastomeric cylinder with three-120 degree chambers. This actuator has seven degrees of freedom: pitch, yaw, stretch, and rotation. Movement is created by increasing the pressure in one or more chambers. If all three chambers are given equal air pressure the actuator extends, but any difference of air pressure between the three chambers results in the actuator bending. Fiber reinforcement prevents damage to the elastomeric cylinder by limiting the strain. The fiber reinforcement angle can be adjusted to give the actuator rotation as internal pressure is increased. Figure 11 is the image of an FMA. Silicone rubber is the ideal material to fabricate the cylindrical actuator and nylon fibers are ideal for the fiber reinforcement. Using multiple FMAs has been shown to create a gripper/claw and also a walking robot.

2.9.1 FMA Model

$$\tan(\theta) = \frac{2P_1 - P_2 - P_3}{\sqrt{3}(P_2 - P_3)} \tag{2.31}$$

$$R = \frac{3E_t I}{A_p \delta \sum_{i=1}^{3} (P_i * \sin\theta_i)} \tag{2.32}$$

$$I = \sum_{i=1}^{3} I_i + \frac{A_0 \delta^2}{2} \tag{2.33}$$

$$\theta_1 = \theta, \theta_2 = \theta + \frac{2}{3}\pi, \theta_3 = \theta - \frac{2}{3}\pi \tag{2.34}$$

$$L = \frac{A_p L_0}{3A_0 E_t} \sum_{i=1}^{3} (P_i + L_0) \tag{2.35}$$

$$\lambda = \frac{L}{R} \tag{2.36}$$

Equations (2.31)-(2.36) are from analysis done by Suzumori et al [15]. Equation (2.31) takes the individual pressure in each channel (P_1, P_2, P_3) and gives the bend angle (θ) of the actuator bends with respect to the x and y axis. The radius of curvature (R) is a function of the Young's modulus of the rubber (E_t), total moment of inertia (I), pressurized cross section area (A_p), the distance between the center axis and actuator center (δ), the internal pressure in each chamber (P_i), and the chamber angles (θ_i). Equation (2.33) and (2.34) gives the total moment of inertia for the actuator and the angles of each chamber. Equation (2.35) gives the length of the FMA at a certain time. Equation (2.36) gives the bending angle (λ) as the length of the actuator divided by the radius of curvature.

2.10 Pleated Pneumatic Artificial Muscle (Pleated PAM)

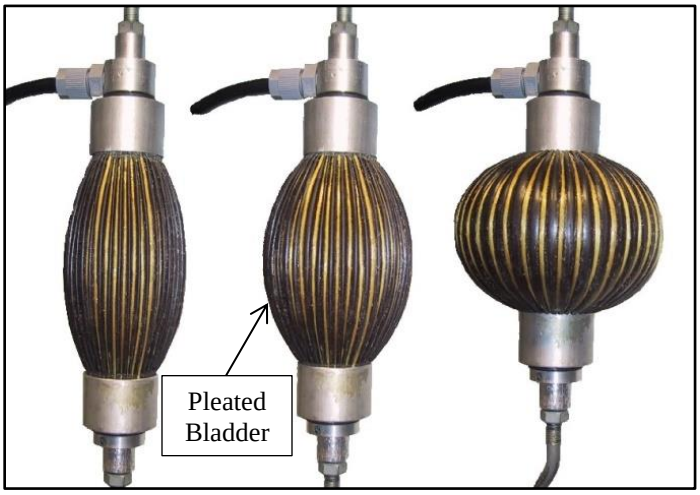

Figure 12: Image of Pleated PAMs

Pleated PAM muscles were found in 1999 by Frank Daerden [16]. This actuator has a membrane with pleats that unfold when the actuators internal air pressure is increased. As the pleats unfold the actuator also bulges in the center. Figure 12 (left to right) shows three stages of increasing internal pressure in the actuator. The pleat depths have to be small in order to minimize parallel stress of the actuator. Parallel stress is the tensile stress that acts tangent to the circular cross-section of the actuator. Parallel stress components reduce the actuators tension force. Daerden suggest the membrane be made of woven fibers and lining to make the membrane air tight. The woven should be Kevlar and Twaron, and polypropylene film is suitable for lining the fibers.

2.10.1 Pleated PAM Model

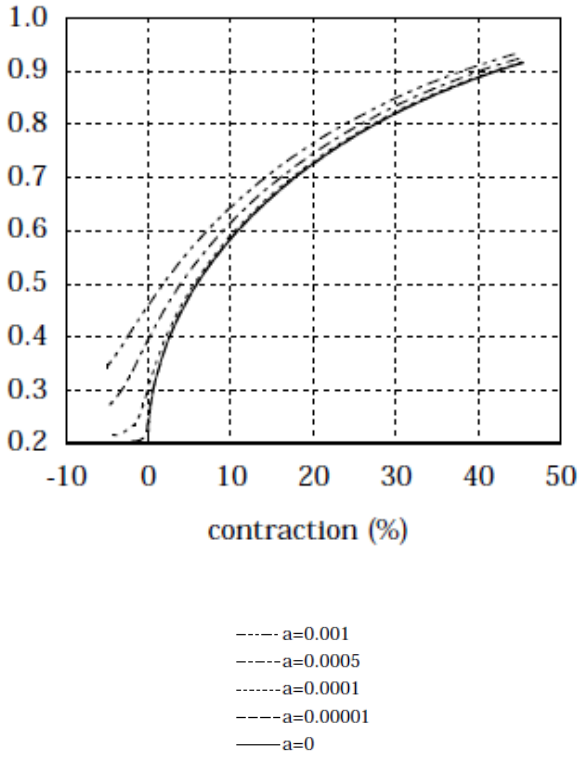

Figure 13: Diameter (dimensionless) vs Contraction [16]

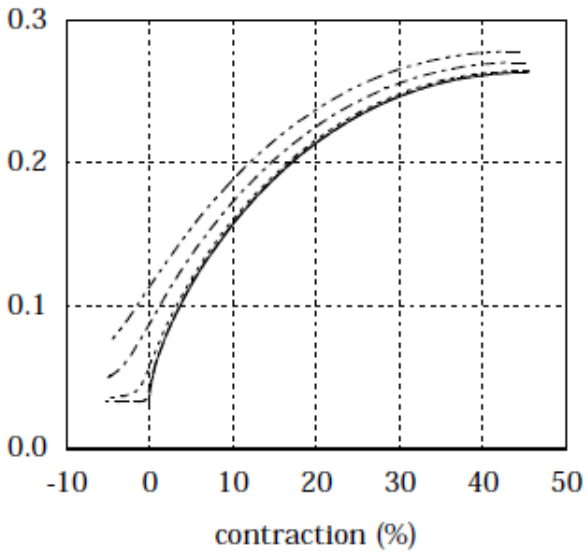

Figure 14: Volume (dimensionless) vs Contraction [16]

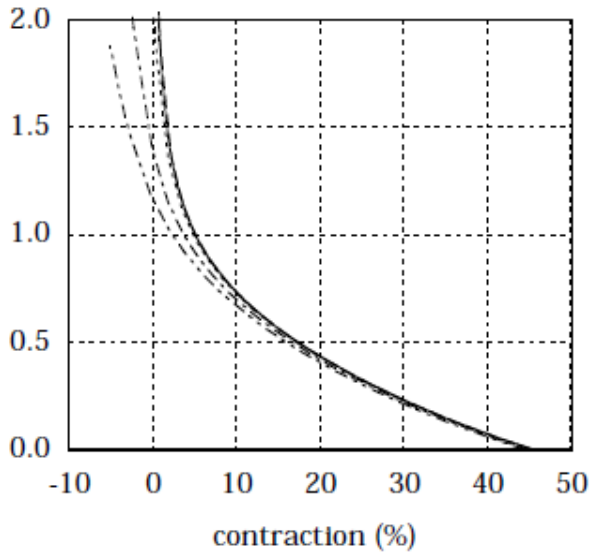

Figure 15: Muscle Tension (dimensionless) vs Contraction [16]

$$\varepsilon = 1 - \frac{2x_0}{l} \tag{2.37}$$

$$D = ld(\varepsilon, \frac{l}{R}, a) \tag{2.38}$$

$$V = l^3 v(\varepsilon, \frac{l}{R}, a) \tag{2.39}$$

$$F_t = pL^2 f_t(\varepsilon, \frac{l}{R}, a) \tag{2.40}$$

The equations are from research done by Frank Daerden on the pleated muscle [16]. Figure 13, Figure 14, and Figure 15 are the diameter (d), volume (v), and tension (f_t) function from Daerden's research on the pleated muscle. These variables are functions of contraction, dimensionless values, and are used to calculate muscle diameter, volume, and tension. Each line of the function represents a different material compliance (bottom of figure 13). For equation

(2.38) (D) is the diameter of the muscle, (l) is the muscle length, and (d) is the diameter function for muscle. Equation (2.39) represents the volume (V) as a function of the length cubed and the volume function of the muscle. Finally, equation (2.40) computes the muscle tension (F_t) as a function of gauge pressure (p), the actuators compressed length (L), and the muscle force function (f_t). Variables d, v, and f_t are functions of contraction (ε), length (l), the muscle radius at rest (R), and membrane compliance (a). Contraction can be found using equation (2.37) with length and initial length (x_0).

2.11 Multi-Module Variable Stiffness Manipulator

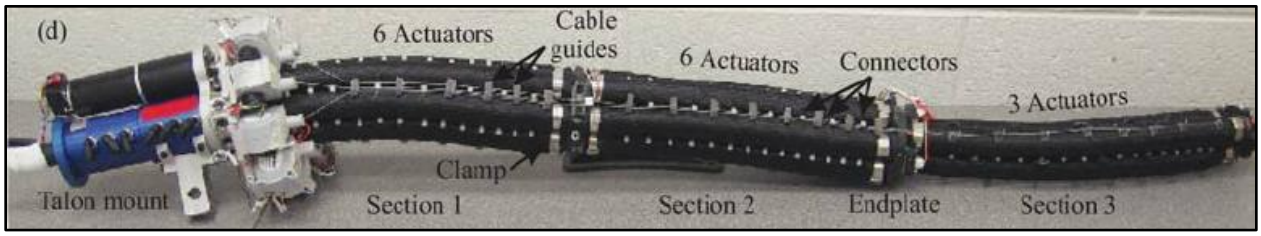

Figure 16: Image of OCTARM manipulator

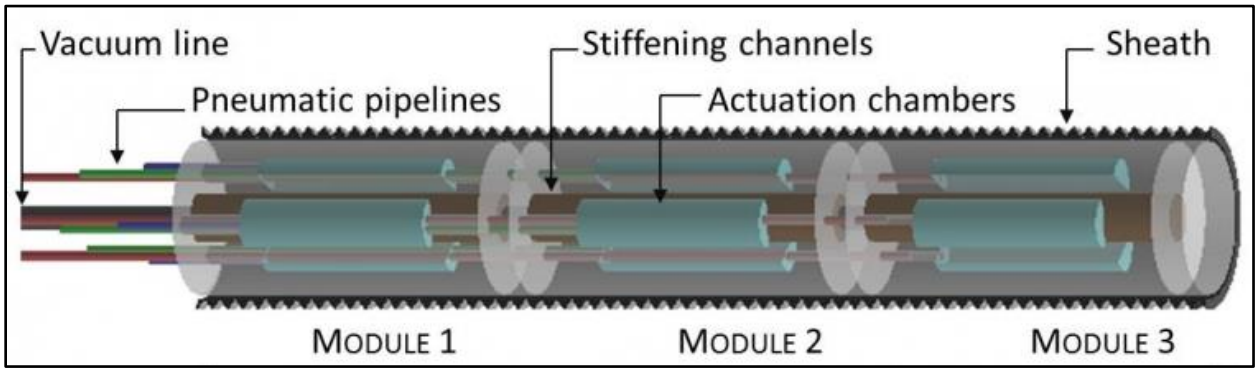

Figure 17: Image of STIFF-FLOP manipulator [17]

Multi-Module variable stiffness manipulators were created in 2004 by Michael B. Pritts and Christopher D. Rahn [18]. There are two approaches to this type of actuator: the Octopus Arm (OCTARM) uses modules of 3-8 McKibben actuators and connecting these modules together [19]; the Stiffness controllable Flexible and Learnable manipulator for surgical Operations (STIFF-FLOP) uses a similar design to the FMA with the addition of a 4^{th} central chamber for granular jamming [20]. These actuators are capable of grabbing objects while distributing evenly around the grasped object. This makes these actuators suitable for grabbing fragile objects that must be handled with caution.

Figure 16 is the OCTARM manipulator which utilizes 15 McKibben actuators by Ian D. Walker et al. This actuator uses 3 sections: the first and second sections have 6 actuators and the third section has 3 actuators. Each section has 3 degrees of freedom: 2 axis bending and extension. More sections and McKibben actuators can be used to increase the degrees of freedom of the robotic arm. This actuator is controlled by changing the internal air pressure in each individual channel or actuator. Walker et al found that increasing the distance between the central axis and the McKibben actuators, increases the moment force exerted by the arm; decreasing this distance increases the arms bending radius.

Figure 17 is the STIFF-FLOP manipulator which utilizes 9 actuation chambers and 3 central stiffening chambers by Iris De Falco et al. This actuator has 3 sections similar to the OCTARM with the exception that each section is the exact same. For each section the 3 outer chambers internal pressure are controlled individually. The central channel is for granular jamming and runs the entire length of the actuator. For granular jamming a granular material is place in the central channel. A vacuum is then applied to this channel causing the channel to conform to the granular material, stiffening the actuator. By increasing this vacuum the stiffness can be

increased. De Falco et al used coffee powder as the granular material and latex is the containing membrane. The rest of the actuator is molded out of Ecoflex silicone rubber.

2.11.1 Multi-Module Variable Stiffness Manipulator Model

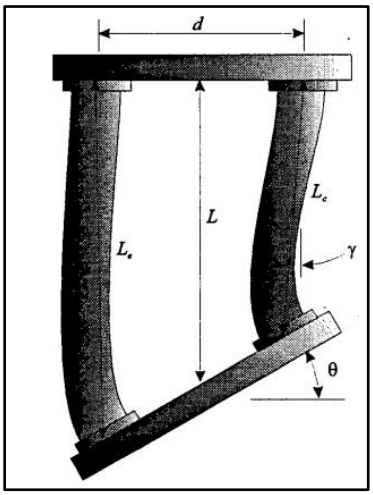

Figure 18: Section of Continuum Robot Manipulator [18]

$$\Delta L^* = \left(1 - \frac{\cos\beta^*}{\cos\alpha}\right) L \tag{2.41}$$

$$\Delta R^* = \left(\frac{\sin\beta^*}{\sin\alpha} - 1\right) R \tag{2.42}$$

$$\alpha_e = \cos^{-1}\left(\frac{\cos\beta^* \cos\alpha_c}{2\cos\alpha_c - \cos\beta^*}\right) \tag{2.43}$$

$$F = \pi R^2 P(2\cot^2\alpha - 1) \tag{2.44}$$

The model was derived by Pritts and Rahn. Figure 18 shows the some of the variables needed to model a section of a continuum robot manipulator utilizing McKibben actuators. Equation (2.41) gives the change in length (ΔL^*) as a function of the center distance (L), final wind angle (β^*),

and initial wind angle (α). Equation (2.42) uses a similar relationship to relate the change in radial expansion (ΔR^*) to the initial muscle radius (R). Subscript c stands for the contraction actuator, right actuator of Figure 18, while the subscript e stands for the extending actuator, left actuator of Figure 18. Equation (2.43) gives the extending actuator wind angle (α_e) as a function of the contracting actuators wind angle (α_c) and the final wind angle. The force of the actuator can be expressed by the initial muscle radius, the internal pressure (P), and the initial wind angle.

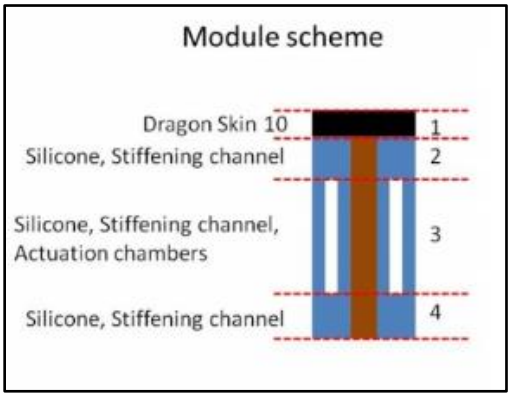

Figure 19: Module Scheme of STIF-FLOP Manipulator [17]

$$\frac{1}{E_{\text{mod}}} = \frac{V_1}{E_1} + \frac{V_2}{E_2} + \frac{V_3}{E_3} \tag{2.45}$$

$$\delta = \frac{PL^3}{3E_{\text{mod}}J_x} + \frac{PL}{GA/\chi} \tag{2.46}$$

$$J_x = J_{sil} - 3J_{ch} - J_{SC} + \frac{J_{SC}}{n} \tag{2.47}$$

$$n = \frac{E_{GJ}}{E_{sil}} \tag{2.48}$$

$$G = \frac{E_{\text{mod}}}{2(1+\nu)} \tag{2.49}$$

The model is from the Soft Robotics Toolkit website. The STIFF-FLOP manipulator utilizes the Reuss model. Figure 19 is a module of the STIFF-FLOP manipulator broken into 4 segments. Layer 1 is a stiff layer, layer 2 and 4 are stiffening channels, and layer 3 includes actuation chambers. The total Young's modulus can be obtained from the volume fractions of each layer (V_i) and the Young's modulus of each layer (E_i). Equation (2.46) relates the deflection of the manipulator (δ) to the applied load (P), the length (L), the total Young's modulus, the area moment of inertia (J_x), the shear modulus (G), cross section area (A), and the shear factor (χ). The area moment of inertia can be found using equation 1.38 where the area moments are needed from each section: subscript (sil) is for the silicone module, (ch) is for the actuation chambers, (SC) is for the stiffening chambers, and (n) is the ratio between the Young's modulus of the granular jamming channel (E_{GJ}) and the Young's modulus of the silicone module (E_{sil}). Equation (2.49) gives the shear modulus of the manipulator as a function of the total Young's modulus and the Poisson's ratio (ν).

2.12 Pneumatic Network Actuator (PneuNet)

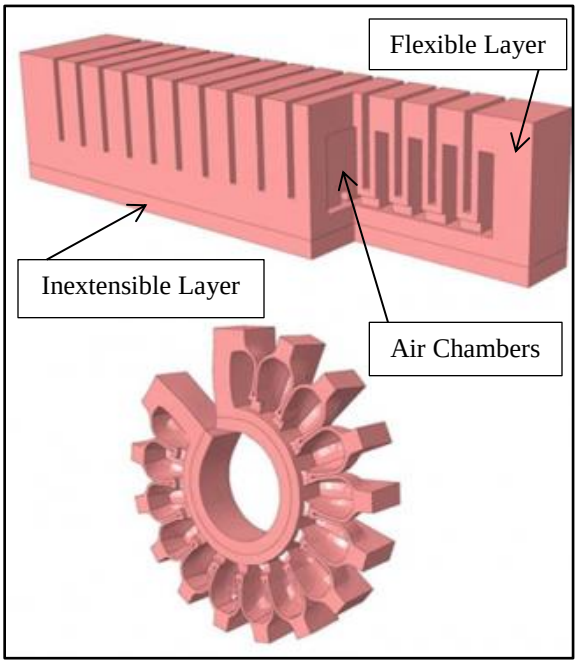

Figure 20: Image of PneuNet actuator

The PneuNet actuator was founded by George M. Whitesides et al. in 2011 [21]. This actuator contains two layers: the first is soft elastomer that contains air chambers that and the second layer is harder elastomer to limit strain. These two layers are sealed together to create a bending actuator that when inflated causes the soft air chambers to expand while the strain limiting layer restricts the actuator to only a bending motion. Figure 20 shows a PneuNet at rest (top) and actuated (bottom). The chamber elastomer layer should be made of a soft flexible rubber such as Ecoflex or Elastosil. For the inextensible layer a stiffer silicone rubber should be used like Sylgard. The inextensible layer can also be made of a softer rubber like Ecoflex or Elastosil with the addition of a paper or fabric layer to limit strain.

The PneuNet actuator can be manipulated in order to create a gripper or a quadrupedal robot. G. Whitesides et al. created a soft gripper by molding 6 PneuNet actuators into a star shape creating

a gripper that can grasp objects by increasing the internal air pressure in all 6 actuators [21]. G. Whitesides et al also created a quadrupedal robot by using 5 Pneunet actuators [22]. There is 1 central actuator with the 4 remaining actuators acting like legs. Crawling is created by varying the internal pressure in the legs and keeping the pressure inside the central actuator constant. Undulation is achieved by varying the air pressure inside the central chamber and the pair of front and the pair of rear legs simultaneously. This quadrupedal robot is capable of crawling over any terrain and undulating under many narrow gaps. G. Whitesides et al also created a more resilient quadrupedal robot that can survive harsh weather environments, exposure to flame, and being run over [23]. By combining individual PneuNet actuators together, more complicated motions can be achieved by this actuator.

2.12.1 PneuNet Model

$$U = \sum_{i=1}^{2} C_i \left(\lambda^2 + \frac{1}{\lambda^2} - 2 \right)^i \tag{2.50}$$

$$\lambda = \frac{\theta}{\sin\theta} \tag{2.51}$$

$$\theta = \sin^{-1}\left(\frac{4ab}{4a^2 + b^2} \right) \tag{2.52}$$

$$\sigma = \frac{\partial U}{\partial \lambda} = \left(\frac{\lambda^4 - 1}{\lambda^3} \right) \left[2C_1 + 4C_2 (\lambda - \frac{1}{\lambda})^2 \right] \tag{2.53}$$

$$\Delta F_E L_W = M_a \Delta P_i \tag{2.54}$$

$$M_a = b^2 \left(2 - \frac{b^2}{b^2 - (2a - d)^2} \right) \tag{2.55}$$

Panagiotis Polygerinos used the Yeoh hyperelastic model to model the PneuNet actuator for a hand rehabilitation glove [24]. Equation (2.50) relates the strain energy density (U) to the principle stretch (λ) and material coefficients (C_1,C_2). The principle stretch is a function of the bend angle of the actuator (θ) from equation (2.51). The bend angle is a function of the PneuNet chamber height (b) and the actuators inflation distance (a). The stress is just the partial derivative of strain energy density taken with respect to the principle stretch. The force exerted (F_E) is a function of the width-justified lever (L_W), the change in internal air pressure (ΔP_i), and (M_a). (M_a) is a constant which shows how an increase in pressure affects the exerted pressure. Polygerinos et al also conducted research on the effects of adjusting various parameters of the PneuNet actuator [25], [26]. They found that increasing the height of the chambers, reducing the number of chambers, and increasing wall thickness, required addition pressure to make the actuator bend. Depending on the application these parameters can be changed in order to best accomplish the task.

2.13 Fiber Reinforced Actuator

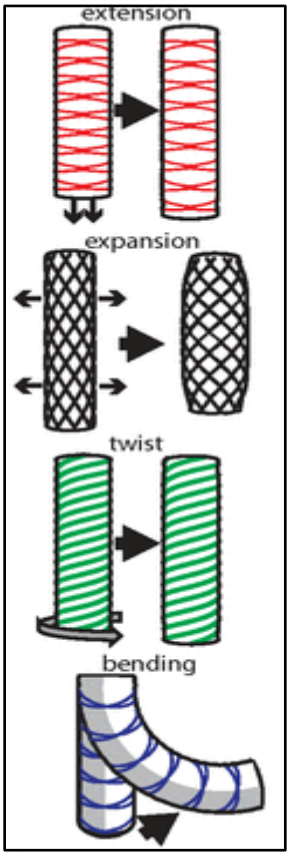

Figure 21: Image of the types of Fiber Reinforced Actuators [27]

Fiber reinforced actuators were first created in 2013 by Joshua Bishop-Moser, Girish Krishnan, and Sridhar Kota [28]. This actuator is an elastic tube with fiber reinforcement running at two different angles or a single fiber running at one angle. As the air pressure inside the bladder is increased, the length of the actuator increases depending on the fiber angle(s) of the actuator. The fiber angle can also cause the actuator to rotate. By attaching a strain limiting layer to part of the bladder, the actuator will bend with increased air pressure. Figure 21 shows the 4 different types of fiber reinforced actuators. The bladder should be made from an elastomeric material like Elastosil with Kevlar string for fiber reinforcement. Paper or fiberglass paper can be used as a

strain limiting layer, which prevents one side or part of the actuator from lengthening when internal pressure is increased. These actuators can be linked together to create a long continuous actuator that can replicate complex movements and have many degrees of freedom.

The effects of varying fiber angle(s) were investigated for the elongation, expansion, and twist by F. Connolly et al [29]. At a zero degree fiber angle (perpendicular to the longitudinal axis) the actuator only extends. As the fiber angle is increased from zero the actuators radial expansion increases. A fiber angle of 90 degrees (parallel to the longitudinal axis) the actuator will only expand radially outward. Connolly et al found that peak twist occurs with a fiber angle of about 30 degrees. Pure extension can also be achieved by having two sets of threads with equal and opposite fiber angle. Adding a second thread at a different angle limits the actuators amount of radial expansion.

2.13.1 Fiber Reinforced Actuator Model

$$W^{(in)} = \frac{\mu}{2}\left(I_1 - 3\right) \tag{2.56}$$

$$W^{(out)} = c_1 W^{(iso)} + c_2 W^{(aniso)} \tag{2.57}$$

$$W^{(iso)} = \frac{\mu}{2}\left(I_1 - 3\right) \tag{2.58}$$

$$W^{(aniso)} = \frac{E\left(\sqrt{I_4} - 1\right)^2}{2} + \frac{E\left(\sqrt{I_6} - 1\right)^2}{2} \tag{2.59}$$

$$\mathbf{S_n} = \begin{pmatrix} 0 \\ \cos\alpha_n \\ \sin\alpha_n \end{pmatrix} \tag{2.60}$$

$$\mathbf{S_n} = \boldsymbol{F}\mathbf{S_n} \tag{2.61}$$

$$I_4 = \mathbf{S_1} \bullet \mathbf{S_1} \tag{2.62}$$

$$I_6 = \mathbf{S_2} \bullet \mathbf{S_2} \tag{2.63}$$

$$W_i = \frac{\partial W}{\partial I_i} \tag{2.64}$$

$$\sigma^{(in)} = 2W_1^{(in)}\boldsymbol{B} - p\boldsymbol{I} \tag{2.65}$$

$$\sigma^{(out)} = 2W_1^{(out)}\boldsymbol{B} + 2W_4^{(out)}\mathbf{S_1} \otimes \mathbf{S_1} + 2W_6^{(out)}\mathbf{S_2} \otimes \mathbf{S_2} - p\boldsymbol{I} \tag{2.66}$$

$$P = \int_{r_i}^{r_m} \frac{\sigma_{\phi\phi}^{(in)} - \sigma_{rr}^{(in)}}{r} dr + \int_{r_m}^{r_o} \frac{\sigma_{\phi\phi}^{(out)} - \sigma_{rr}^{(out)}}{r} dr \tag{2.67}$$

$$N = 2\pi \int_{r_i}^{r_m} \sigma_{zz}^{(in)} r dr + 2\pi \int_{r_m}^{r_o} \sigma_{zz}^{(out)} r dr = P\pi r_i^2 \tag{2.68}$$

$$M = 2\pi \int_{r_i}^{r_m} \sigma_{\phi z}^{(in)} r^2 dr + 2\pi \int_{r_m}^{r_o} \sigma_{\phi z}^{(out)} r^2 dr = 0 \tag{2.69}$$

$$\boldsymbol{F} = \begin{pmatrix} \dfrac{R}{r\lambda_z} & 0 & 0 \\ 0 & \dfrac{r}{R} & r\tau\lambda_z \\ 0 & 0 & \lambda_z \\ & & \end{pmatrix} \tag{2.70}$$

$$M_{cap} = 2PR_i^2 \int_0^{\pi} \sin^2\phi \, abs\left(R_i \cos\bar{\phi} - R_i \cos\phi\right) d\phi \tag{2.71}$$

$$M_{mat} = \iint \frac{\sigma_{zz}\left(R_i + \tau\right)\left(R_i \cos\bar{\phi} - \left(R_i + \tau\right)\cos\phi\right)}{\lambda_z} d\phi d\tau \tag{2.72}$$

$$P = \frac{\iint \lambda_z^{-1}\sigma_{zz}\left(R_i + \tau\right)\left(R_o \cos\bar{\phi} - \left(R_i + \tau\right)\cos\phi\right) d\phi d\tau}{2R_i^2 \int_0^{\pi} \sin^2\phi \, abs\left(R_i \cos\bar{\phi} - R_i \cos\phi\right) d\phi} \tag{2.73}$$

$$F = \begin{pmatrix} \lambda_z\left(\phi\right)^{-1} & 0 & 0 \\ 0 & 1 & 0 \\ 0 & 0 & \lambda_z\left(\phi\right) \end{pmatrix} \tag{2.74}$$

A model for the fiber reinforced actuator was created by F. Connolly et al [27].The strain energies of the inner and outer layers are represented by ($W^{(in)}$) and ($W^{(out)}$). Equations (2.60) and (2.61) result in two separate matrices: one for the thread (n=1) and the other for the second thread (n=2). Equations (2.65) and (2.66) are used to find the Cauchy stress tensor ($\sigma^{(in)}$) and ($\sigma^{(out)}$). Equations (2.67)-(2.69) are for an extension, expansion, or twist actuator; equations (2.72)-(2.74) are for a bending actuator. For both situations the applied pressure (P), axial load (N), axial moment (M), and deformation gradient (**F**) are used to solve for the axial stretch (λ_z), twist (τ), and inner radius (r_i). The applied pressure, axial load, and axial moment are found using values from the in and out Cauchy stress tensors.

Chapter 3: Electric Electroactive Polymers (Electric EAP)

3.1 Dielectric Elastomer Actuator (DEA)

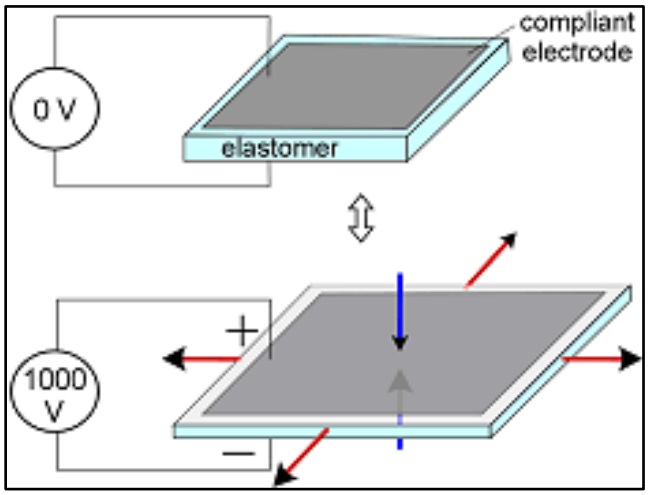

Figure 22: Image of DEA

Dielectric Elastomer Actuators were first discovered in 1880 by Wilhelm Conrad Roentgen [30]. The actuator consist of an elastomer film sandwiched between two compliant electrodes. When a voltage is applied the actuator flattens while the surface area increases. Figure 22 shows a DEA when no voltage is applied (top) and when a voltage is applied (bottom). The flattening characteristics of the DEA can be manipulated by changing the geometry to form a linear actuator. There are multiple ways to make DEAs: the first is to apply compliant electrodes to the inside and outside of PDMS tube [31], the second to make multi-layer stack of PDMS rubber and compliant electrode, and finally [32], place compliant electrode on a strip of PDMS and fold it to create a folded DEA [32]. A dielectric material has to have a high dielectric constant and low elastic stiffness. Good examples of dielectric materials are PDMS rubber and VBH tape. PDMS rubber is capable of being molded to create DEAs of different shapes. Carbon conductive grease

and carbon black powder are suitable compliant electrodes. DEAs require a large voltage to trigger actuation, around 100 volts per micron.

3.1.1 DEA Model

$$p = \varepsilon_0 \varepsilon_r \left(\frac{V}{d} \right)^2 \tag{3.1}$$

$$C = \frac{2\pi \varepsilon_0 \varepsilon_r L}{\ln\left(\frac{b}{a} \right)} \tag{3.2}$$

$$p_a = \frac{|\nabla U|}{2\pi a L} \tag{3.3}$$

$$p_b = \frac{|\nabla U|}{2\pi b L} \tag{3.4}$$

$$U = \frac{1}{2} C V^2 = \frac{\pi \varepsilon_0 \varepsilon_r L V^2}{\ln\left(\frac{b}{a} \right)} \tag{3.5}$$

$$|\nabla U| = \sqrt{\left(\frac{\partial U}{\partial a} \right)^2 + \left(\frac{\partial U}{\partial b} \right)^2 + \left(\frac{\partial U}{\partial L} \right)^2} \tag{3.6}$$

The equations come from Federico Carpi and Danilo De Rossi's analysis of cylindrical dielectric elastomer actuators [31]. Equation (3.1) is a general equation for all dielectric elastomers. Electrostatic pressure is represents as a function of relative dielectric constant (ε_r), the dielectric permittivity constant in a vacuum (ε_0), applied voltage (V), and actuator thickness (d). Equation (3.2) solves for the capacitance of the actuator. Variable (a) is the radius of the outer cylinder surface, (b) is the diameter of the inner cylinder surface, and (L) the initial electrode length. The

variables (p_a) and (p_b) are the electrostatic pressures exerted at the inner electrode surface and outside electrode surface while (U) is the elastic energy. For equations (3.3) and (3.4) the magnitude of the elastic energy is needed to solve for the electrostatic pressures.

3.2 Ferroelectric Polymer Actuator

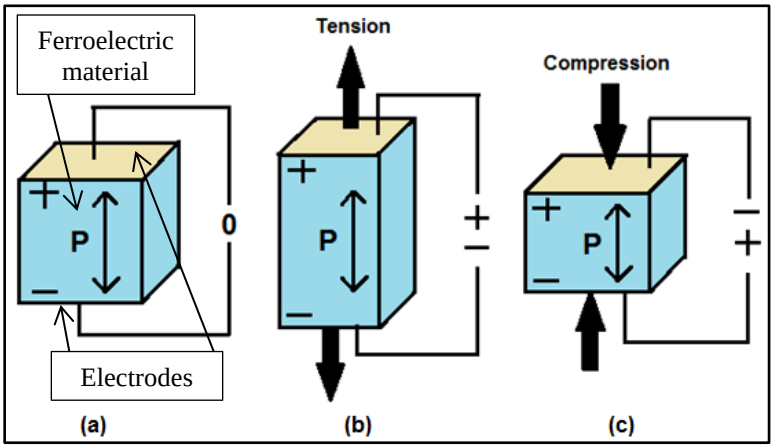

Figure 23: Image of Ferroelectric Polymer

Piezoelectricity was discovered in 1880 by Pierre and Paul-Jacques Curie [33]. Piezoelectric polymers and ferroelectric polymers were discovered in 1969 by Heiji Kawai [2]. These polymers can generate voltage when a stress is applied to them this is known as the direct effect. These polymers can also generate a stress when a voltage is applied to them this is known as the converse effect and was discovered in 1881. Figure 23 shows that a piezoelectric actuator can be put into either tension or compression by applying a voltage to the actuator. Ferroelectricity is a type of piezoelectricity. A piezoelectric material has a measureable current when stressed due to polarization. When an electric field is applied, ferroelectric materials reverse their dipole moment direction [2]. Polyvinyl fluoride (PVF) and polyvinylidene fluoride (PVDF) are examples of ferroelectric polymers.

3.2.1 Ferroelectric Polymer Actuator Model

$$\boldsymbol{\varepsilon} = \boldsymbol{s}^{E}\boldsymbol{\sigma} + \boldsymbol{d}^{c}E \tag{3.7}$$

$$\boldsymbol{D} = \boldsymbol{d}^{d}\boldsymbol{\sigma} + \boldsymbol{e}^{\sigma}E \tag{3.8}$$

$$\sigma = \frac{F}{A} = \frac{F}{bt} \tag{3.9}$$

$$E = \frac{V}{t} \tag{3.10}$$

The model for piezoelectricity is from the IEEE standard on piezoelectricity [34]. Equation (3.7) is called the actuator equation and equation (3.8) is called the sensor equation. The actuator equation gives the strain (ε) as a function of elastic compliance (s^E), stress (σ), the piezoelectric coefficient (d^c), and the electric field (E). The sensor equation relates the electric displacement (D) to the piezoelectric coefficient (d^d), stress, electric permittivity (e^σ), and electric field. Equation (3.9) gives the stress as a function of Force (F) and Area (A); equation (3.10) gives the electric field as a function of voltage (V) and thickness (t).

3.3 Electro-Viscoelastic Elastomer

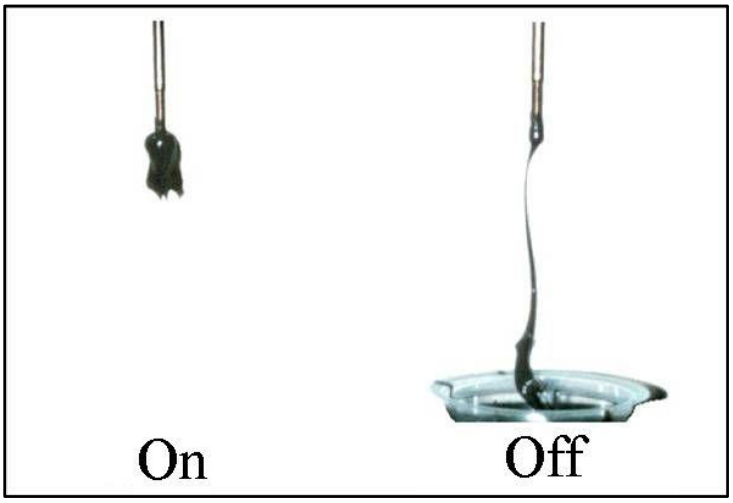

Figure 24: Image of Electro-Viscoelastic Elastomers

Electro-Viscoelastic Elastomers change their shear modulus in response to an applied electric field. Electro-Viscoelastic Elastomers were discovered in 1950 by A. Katchalsky et al [35]. Before curing electro-viscoelastic elastomers behave like ER fluids. During curing, an electric field is applied to the elastomer that fixes the elastomers polar phase. When an electric field is applied to the elastomer its shear modulus is increased, making the elastomer behave like a solid. Increasing the electric field increases the shear modulus of the elastomer. Figure 24 shows an electro-viscoelastic elastomer when a voltage is applied (left) and when no voltage is applied (right). Tohru Shiga created an electro-viscoelastic elastomer from composite gels and poly-methacrylic acid cobalt (II) salt (PMACo) particles [36]. Electro-Viscoelastic elastomers are an alternative for ER fluids. Variable damping is the best application for these actuators.

3.3.1 Electro-Viscoelastic Elastomer Model

$$\mu = 4\pi r^3 \varepsilon_0 \varepsilon_1 \kappa E \tag{3.11}$$

$$\kappa = \frac{\varepsilon_2 - \varepsilon_1}{\varepsilon_2 + 2\varepsilon_1} \tag{3.12}$$

$$F(R,\theta) = R_0 \left\{ \left(\frac{2r}{R} \right)^4 [(3\cos\theta - 1)\hat{\boldsymbol{e}}_r + \sin(2\theta)\hat{\boldsymbol{e}}_\theta] \right\} \tag{3.13}$$

$$\Delta G = \left(\frac{9}{4} \right) C\varepsilon_1 \kappa^2 E^2 \tag{3.14}$$

The equation were derived by Tohru Shiga [36]. These equations apply to two polarized particles in a viscoelastic gel subjected to an electric field. The point dipole moment (μ) where (r) is the radius of a particle, (ε_0) is the permittivity in a vacuum, (ε_1) is the dielectric constant of the first particle, (ε_2) is the dielectric constant of the second particle, and (E) is the applied electric field. For equation (3.13) (F) is the dipole-dipole interaction force (F), (R_0) is the initial distance between the particles, (R) is the current distance between particles, (θ) is the angle between particles. The change in shear modulus (ΔG) due to the applied electric field can be found using equation (3.14).

3.4 Liquid Crystal Elastomers (LCE)

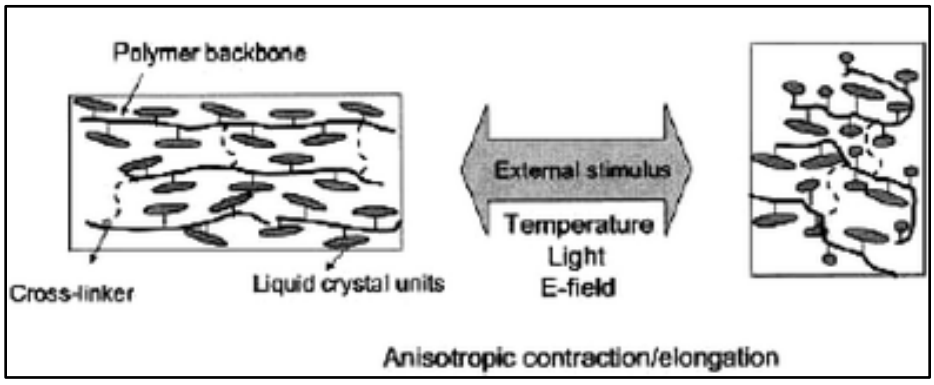

Figure 25: Image of LCE

Discovered in 1981 by Heino Finkelmann, Hans J. Kock, and Gunther Rehage, liquid crystal elastomers experience elongation or contraction by transitioning between nematic and isotropic phases [37]. Elongation occurs when an LCE transitions from an isotropic to nematic phase, and shrinks when transitioning from a nematic to isotropic phases. The performance of these actuators can be affected by changing the liquid crystalline phase, crosslinking density, polymer backbone flexibility, or the coupling between the backbone polymer, liquid crystal group, and external stimuli [38]. Figure 25 shows the three different ways LCEs can be actuated: temperature, light, and electric field. These three external stimuli are discussed in the following paragraphs.

Temperature activated LCEs change their shape due to a change in temperature. This is due to the bonds between the liquid crystal side chain and the backbone polymer. At the liquid crystalline to isotropic phase transformation temperature, the elastomer transitions from anisotropic to isotropic causing the bonds to shorten [39], [40]. As the temperature increases these materials strain decreases while the generate force increases. Light activated LCEs change shape due to photoisomerizing. When exposed to UV light photoisomerizable molecule rods are absorber causing them to bend [41]. As the time exposed to UV light increases the elastomer contracts. Finkelmann and Nishikawa created one of these elastomers using (PHMS) as a backbone polymer, M4OCH_3 as the mesogenic rod, and M4CN as a side chain. Electrically activated LCEs behave similarly to ferroelectric polymers. These LCEs have a helical structure formed by the free energy in the LCE. Ferroelectric LCEs (FLCEs) are created by unwinding this structure, preventing it from recovering, and avoiding flow in the LCE under stress [42]. Lehman et al created an FLCE using polysiloxane as the back bone polymer and two different chiral liquid cryatal copolymers.

3.4.1 LCE Model

$$\lambda = \frac{L}{L_{iso}} \tag{3.15}$$

$$S = -\frac{\sigma}{U} + \left(\frac{\mu}{U}\right)\lambda \tag{3.16}$$

The model for temperature driven LCEs was derived by Hendrik Wermter and Heino Finkelmann [40]. The elastic modulus (μ), the mechanical field (σ), the deformation (λ), and the cross coupling coefficient (U) are used to find the nematic order (S). Wermter and Finkelmann created one of these actuators using PHMS as the backbone polymer, 4-but-3-enyloxybenzoic acid 4-methoxyphenyl ester as the mesogen chain, and 1-(4-hydroxy-4-biphenyl)-2-[4-(10-undecenyloxy)phenyl]butane as a cross-linking polymer.

$$e_{T_0} = \frac{L'\left(T_0 + \gamma T_{ni} t\right)}{L\left(T_0\right)} \gamma T^* \tag{3.17}$$

$$\rho(t) = \frac{\rho_0}{1+\tau\eta}\left\{1 + \tau\eta \exp\left[\frac{-t\left(1+\tau\eta\right)}{\tau}\right]\right\} \tag{3.18}$$

The equations above are from work on light activated LCEs by H. Finkelmann and E Nishikawa [41]. The relative contraction is a function of the length, change in length, and the temperature. The elastomer density is expressed as a function of time.

$$\frac{\Delta L}{2} = k_1 \hat{U} \tag{3.19}$$

$$k_1 = a + 2bU_{dc} \tag{3.20}$$

$$\frac{\Delta L}{2} = k_2 \hat{U}^2 \tag{3.21}$$

$$k_2 = \frac{b}{2} \tag{3.22}$$

$$\frac{\Delta L}{2} = aU(t) + bU^2(t) \tag{3.23}$$

$$U(t) = U_{dc} + \hat{U}\cos(\omega t) \tag{3.24}$$

$$\frac{\Delta L}{2}(\omega, 2\omega) = (a + 2bU_{dc})\hat{U}\cos(\omega t) + \frac{b}{2}\hat{U}^2\cos(2\omega t) + const. \tag{3.25}$$

FLCEs can be modeled using the equations from W. Lehmann, L. Hartmann, and F. Kremer [42]. Variables (k_1) and (k_2) are solved from the measured amplitude ($\frac{\Delta L}{2}$) and the applied ac voltage ($\widehat{U}$), and a superimposed applied dc voltage (U_{dc}). From these values (a) and (b) can be solved and plugged into equation (3.23) or (3.25) to get an expression for the amplitude.

3.5 Electrostrictive Graft Elastomers

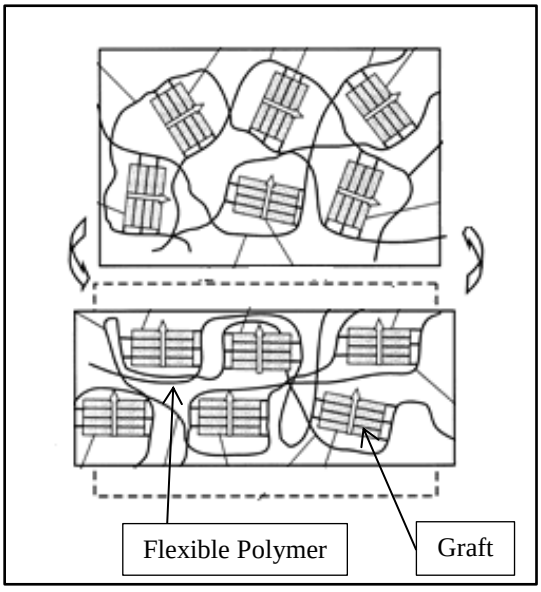

Figure 26: Image of Electrostrictive Graft Elastomer

Electrostrictive graft Elastomers were created in 1998 by Ji Su, Jocelyn S. Harrison, and Terry L. St. Clair [43]. When no electric field is applied to the elastomer, the grafts are randomly oriented (top) but when an electric field is applied the grafts orient themselves causing the elastomer to flatten (bottom) as shown in Figure 26. Electrostrictive graft elastomers are made from two components: a flexible polymer and a grafted crystalline polymer. Su created the graft elastomer by mixing graft elastomer powder to N,N-Dimethylformamide, and gold was used as the compliant electrodes.

3.5.1 Electrostrictive Graft Elastomers Model

$$S_L = 2S_T = 2d\left(\frac{1}{R}\right) = \frac{4dL}{L^2 + l^2} \tag{3.26}$$

$$S_{electro} = -Q\varepsilon_0^2 E^2 (K-1)^2 \tag{3.27}$$

$$S_{Maxwell} = -s\varepsilon_0^2 K \frac{E^2}{2} \tag{3.28}$$

$$S = S_{electro} + S_{Maxwell} \tag{3.29}$$

The model is from J. Su et al report on electrostrictive graft elastomers [44]. In equation (3.26) (S_L) is the longitudinal strain of the elastomers active layer, (S_T) is the transversal strain of the elastomers active layer, (d) is the distance between the active and non-active layers, ($\frac{1}{R}$) is the bending curvature of the actuator, (L) is the tip deflection in the in-surface direction, and (l) is the tip defection in the off-surface direction. Equations (3.27)and (3.28) give the electrostriction stress ($S_{electro}$) and Maxwell stress ($S_{Maxwell}$) where variable (Q) is electrostrictive coefficient, (K) is the dielectric coefficient, (E) is the applied electric field, (ε_0) is the vacuum permittivity,

and (s) is the mechanical compliance. The total strain (S) is equal to the electrostriction stress and the Maxwell stress combined.

3.6 Electrostrictive Paper (EA Pap)

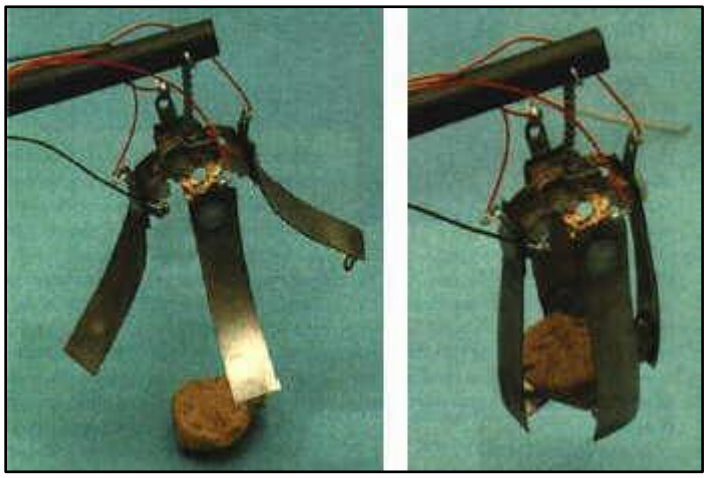

Figure 27: Image of EA Pap actuator

Discovered in 2000 by Jaehwan Kim, Jung-Yup Kim, and Soonja Choe, the tip of an EA Pap actuator deflects when a voltage is applied [45]. When a voltage is applied to the actuator, it bends this is due to electrostatic forces and intermolecular interaction of the glue [43]. Greater bending displacement is achieved by increasing the applied voltage. Kim et al created this actuator by gluing two pieces of silver laminated paper together, using emulsion adhesive, and laminating aluminum foil over each laminated paper. Figure 27 shows a claw created by using 4 EA Pap actuators. The claws open when a voltage is applied to them (left), and they close when the voltage is removed (right).

Chapter 4: Ionic Electroactive Polymer (Ioninc EAP)

4.1 Conductive Polymers

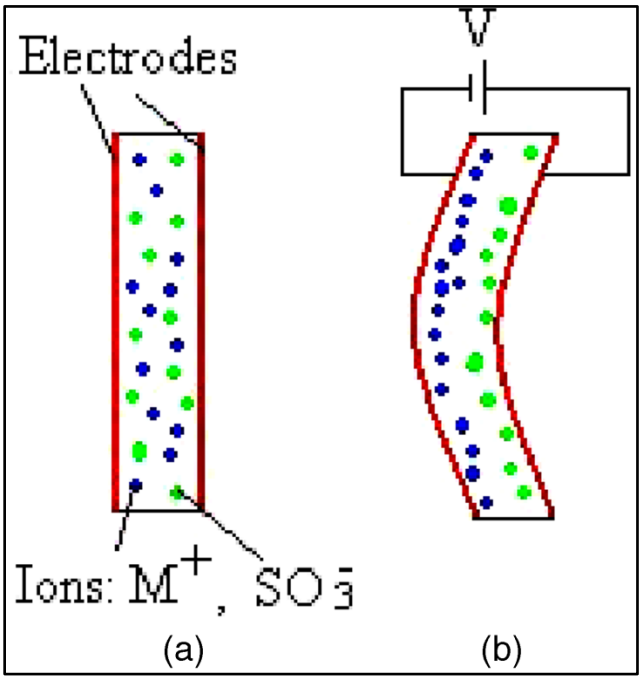

Figure 28: Image of Conductive Polymer

Records suggest conductive polymers were founded in 1862 by Henry Letheby [46]. This actuator consists of electrolyte layer and a conductive polymer layer (bilayer). It can also be made from electrolyte sandwiched in between two conductive polymer electrodes (trilayer). Volume changes occur due to oxidation and reduction taking place at the electrodes. Oxidation causes the conductive polymer layer to expand while reduction causes the conductive polymer to shrink. For the bilayer actuator oxidation causes the actuator to bend in one direction and the actuator bends the other direction during reduction. For the trilayer setup oxidation occurs at one conductive polymer layer and reduction occurs at the other polymer layer, causing bending in one direction. Bending in the other direction is achieved by applying the opposite potential.

Figure 28 shows when a voltage is applied the positive ions move toward the cathode while the negative ions move toward the anode. Some conductive polymers include polypyrrole, polyaniline, and polythiophenes. The electrolyte can either be a liquid of an electrolyte film. Bar-Cohens review of electroactive polymers states that thinner actuators bend faster but produce a lower force; thicker actuators bend slower but produce a higher force [43].

4.1.1 Conductive Polymer Model

$$n = \frac{Q}{e} \tag{4.1}$$

$$\Delta c = \frac{\Delta Q}{wzF} \tag{4.2}$$

$$\frac{\Delta V}{w} = \frac{nV_a}{w} \tag{4.3}$$

$$\Pi = icRT \tag{4.4}$$

$$\frac{\Delta V}{w} = \frac{nV_a + mV_w}{w} = \Delta c_a V_a + \Delta c_{aq} V_{aq} \tag{4.5}$$

$$angle(t) = angle_0 + kQ(t) \tag{4.6}$$

$$\omega(t) = \frac{d(angle(t))}{dt} = k\frac{dQ(t)}{dt} = kI(t) \tag{4.7}$$

The principle equations are from Electromechanically Active Polymers by Federico Carpi [47]. Equation (4.1) is Faraday's law, where (n) is the number of ions exchanged between electrolyte and polymer, (Q) is the consumed charge, and (e) is the charge of an electron. The change in concentration (Δc) depends on change in charge (ΔQ), weight of the polymer (w), (z), and

Faraday's constant (F). The change in volume (ΔV) per polymer mass (w) depends on the number of ions and the volume occupied by one ion (V_a). Equation (4.4) is Van't Hoff's equation where the osmotic pressure (Π) equals the product of Van't Hoff factor (i), concentration (c), the gas constant (R), and temperature (T). For equation (4.5) when reactions occur, water and ions are exchanged. The variable (V_a) is the anion volume, (Δc_a) is the ionic specific concentration, (V_{aq}) is the water volume, and (Δc_{aq}) is the water molecule specific concentration. Equation (4.6) and (4.7) describe the angle deflection and angular velocity of the actuator (ω). The angle at any time can be expressed using the actuators initial angle ($angle_0$), the coulo-dynamic constant (k), and the charge (Q). the angular velocity can be obtained from either the derivative of the angle function or the product of the derivative of the charge function and the coulo-dynamic constant. The derivative of the charge function is the current (I).

4.2 Electro-Rheological Fluids (ER Fluids)

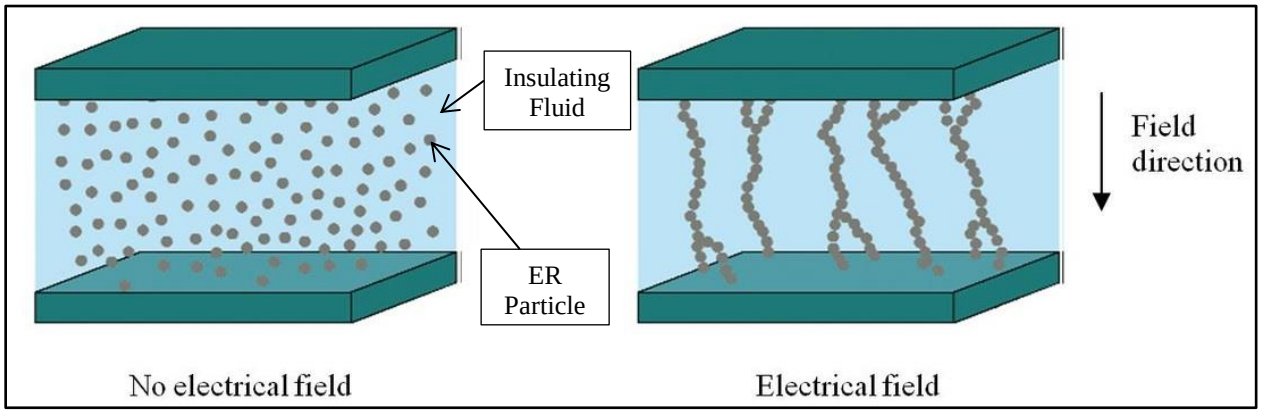

Figure 29: Image of ER Fluid

The electro-rheological (ER) effect was first discovered in 1940s by Willis Winslow [33]. These fluids have particles that can change the fluids viscosity when subjected to an electric field. The fluid is low-viscosity insulating fluid while the particles are non-conducting while having a

diameter of 1-10 μm [48]. Fluid such as mineral oil, silicone oil, or paraffin oil; particles such as corn starch, silica spheres or alumino-silicate can be used to create ER fluid. Figure 29 shows particles submerged in fluid, when voltage is applied the particles for, chains that align with the electric field increasing the fluids viscosity. When the electric field is off the ER fluids behave like a liquid but when an electric field is applied the fluid behaves more like a gel.

4.2.1 ER Fluid Model

$$x(t) = X_0 \cos(\omega t) \tag{4.8}$$

$$\Delta W = \int_{cycle} F dx = \int_0^{2\pi/\omega} F \dot{x} dt \tag{4.9}$$

$$F = c_{eq} \dot{x} = -c_{eq} X_0 \omega \sin(\omega t) \tag{4.10}$$

$$\Delta W = \int_0^{2\pi/\omega} c_{eq} \dot{x} \dot{x} dt = c_{eq} X_0^2 \omega^2 \int_0^{2\pi/\omega} \sin^2(\omega t) dt = \pi c_{eq} X_0^2 \omega \tag{4.11}$$

$$\tau = \tau_y \operatorname{sgn}(\dot{\gamma}) + \mu \dot{\gamma} \tag{4.12}$$

$$F = F_c \operatorname{sgn}(\dot{x}) + c_o \dot{x} \tag{4.13}$$

The equations for ER fluids come from Inderjit Chopra and Javant Sirohi [48]. Equation (4.8) is the position as a function of amplitude (X_0) and frequency (ω). The dissipated energy (ΔW) is the integral of force (F) and velocity ($\dot{x}$), the derivative of the position. The force is the product of the damping coefficient (c_{eq}) and the velocity. Equations (4.12) and (4.13) are the Bingham Plastic model. The shear stress (τ) is a function of yield shear stress (τ_y), the shear strain rate ($\dot{\gamma}$), and the viscosity (μ). The damping force (F) is a function of Coulomb friction force (F_c), viscous damping coefficient (c_o), and velocity. Equation (4.12) is only applicable when the shear stress is

greater than the yield shear stress; equation (4.13) is only applicable when the damping force is greater than the Coulomb friction force.

4.3 Polymer Gels

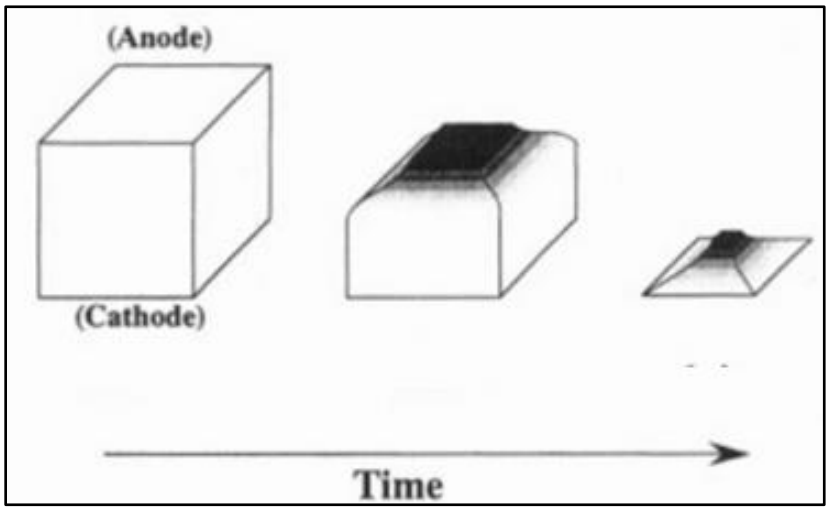

Figure 30: Image of Polymer Gel [49]

Polymer gels were discovered in 1940s by K. Katchalsky et al [50]. Polyacrylonitrile and polyacrylamide are examples of ionic polymer gels. These materials can be actuated by changing between acid and alkaline solutions, or electrically. The cathode becomes more alkaline and the anode becomes more acidic. By changing from either an acid or alkaline solution causes the gel to swell or shrink. Figure 30 shows a polyanionic gel swelling at the cathode and contracting at the anode. For a cationic gel the swelling would occur at the anode while contraction occurs at the cathode.

4.3.1 Polymer Gel Model

$$F_f = \eta 2\pi r[dv(r)/dr]_r - \eta 2\pi(r+dr)[dv(r)/dr]_{(r+dr)} \tag{4.14}$$

$$F_e = 2\pi r dr \rho(r) E \tag{4.15}$$

$$2\pi r dr\rho(r)E = \eta 2\pi r[dv(r)/dr]_r - \eta 2\pi(r+dr)[dv(r)/dr]_{(r+dr)} \tag{4.16}$$

$$\rho(r)E = -\eta\Delta v(r) \tag{4.17}$$

$$\rho(r) = (2kT\varepsilon\beta^2/e)/\{r^2\sin^2[-\tan^{-1}\beta + \beta\ln(r/r_o)]\} \tag{4.18}$$

$$v(r) = (\varepsilon EkT/e\eta)\ln\{(r/r_i)\sin[-\tan^{-1}\beta + \beta\ln(r/r_o)]/\sin[\tan^{-1}\beta + \beta\ln(r_i/r_o)]\}^2 \tag{4.19}$$

$$\lambda = \frac{\left(1+\beta^2\right)}{\left[1-\beta\cot(\beta s)\right]} \tag{4.20}$$

$$\lambda = \frac{\alpha e^2}{4\pi\varepsilon bkT} \tag{4.21}$$

$$s = \ln\left(\frac{r_i}{r_o}\right) \tag{4.22}$$

$$dQ = \rho(r)v(r)dS = 2\pi r\rho(r)v(r)dr \tag{4.23}$$

$$u_{av} = \{\int_{r_i}^{r_o}[2\pi r/\rho(r)]dr\}/\pi(r_o^2 - r_i^2) \tag{4.24}$$

$$\frac{W}{W_W} = 1 - \int_0^Q u_{av}\frac{dQ}{L_0 S} = 1 - \frac{u_{av}Q}{L_0 S} \tag{4.25}$$

The model is from J.P. Gong et al analysis on polyelectrolyte gels [49]. The frictional force (F_f) is found from the viscosity (η), the distance between the center and inner cylinder (r), the distance between two concentric cylinders (dr) and water flow velocity (v(r)). In equation (4.15) (F_e) is the electrical force, local charge density (ρ(r)), and electric field (E). From equations (4.18) and (4.19) (k) is the Boltzmann constant, temperature (T), dielectric constant of water (ε),

charge of an electron (e), inner radius (r_i), and outer radius (r_o). The variable (β) is found using equation (4.20) and (4.21), where (α) is the degree of ionization, (b) is the distance between ion groups on the polyanion, and (s) is solved using equation (4.22). Equation (4.23) gives the rate of charge (dQ). Equation (4.20) give the average charge (u_{av}) of one macroion. Equation (4.25) is the specific weight ($\frac{W}{W_W}$) as a function of average charge, the amount of charge (Q), initial gel length (L_0), and the cross section area (S).

4.4 Ionomeric Polymer-Metal Composites (IPMC)

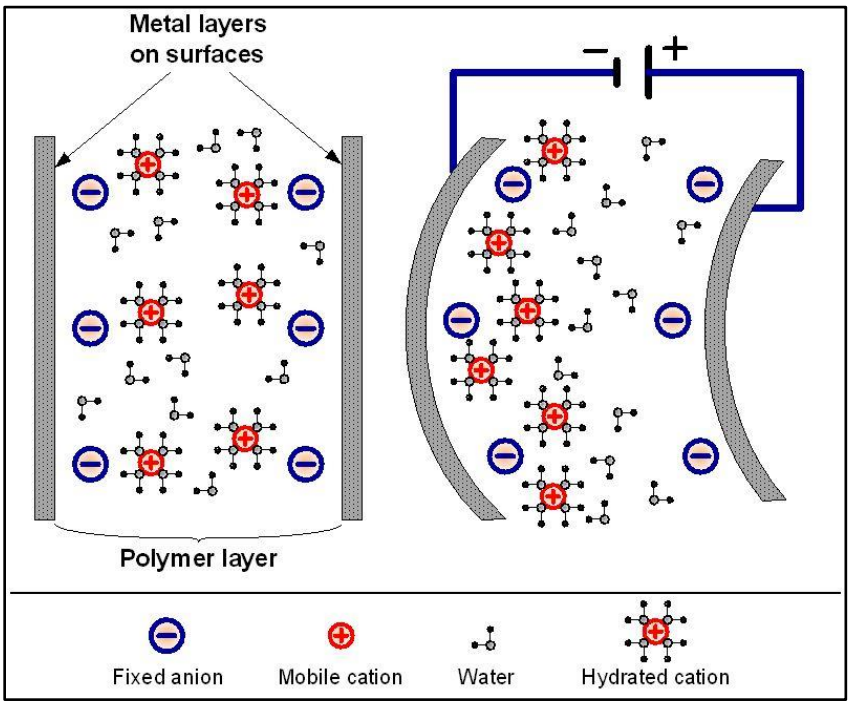

Figure 31: Image of IPMC

Ionomeric polymer-metal composites (IPMC) were discovered in 1992 by three different research groups: K. Ogura et al, M. Shahinpoor, and Sadeghipour et al [33]. When a voltage is applied IPMCs bend due to mobile cations in the polymer networks. Hydrated cations move toward the cathode when an electric field is applied, shown in Figure 31. IPMC are made using

two polymers: perfluorosulfonate (Nafion) and perfluorocaboxylate (Flemion), and conductive electrodes made from platinum or gold [43].

4.4.1 IPMC Model

$$\sigma^T = \sigma + \sigma^* \tag{4.26}$$

$$\sigma^* = \sigma^e + \sigma^o \tag{4.27}$$

$$\sigma^e = -k_0 \rho \mathbf{1} \tag{4.28}$$

$$k_0 = \frac{e}{4\pi\kappa_e r_c^2}\frac{r_d^3}{\pi r_e^2} \tag{4.29}$$

$$\rho = (C^+ - C^-)F \tag{4.30}$$

$$\sigma^o = -\boldsymbol{C}_{\boldsymbol{p}}\varepsilon^o \tag{4.31}$$

$$\Delta F_i = \frac{-e}{4\pi\kappa_e r_c^2}(C^+ - C^-)F r_d^3 \tag{4.32}$$

The model was derived by Sia Nemat-Nasser and Jiang Yu Li[51]. In equation (4.26) the total stress (σ^T) is the addition of the polymer stress (σ) and the eigenstress (σ^*). The eigenstress is the addition of the electrostatic stress (σ^e) and the osmotic stress (σ^o). The electrostatic stress is the product of the charge density (ρ), and the identity tensor (**1**). The variable (k_0) is calculated using the charge of one electron (e), polymer dielectric constant (κ_e), cluster radius (r_c), cluster distance (r_d), and effective radius (r_e). For charge density (C^+) is the positive ion density, (C^-) is the negative ion density, and (F) is Faraday's constant. The osmotic stress is the product of the

elastic stiffness tensor ($\boldsymbol{C_p}$) and the volume strain from water redistribution (ε^o). Equation (4.32) calculates the change in electrostatic interaction force (ΔF_i).

4.5 Carbon Nanotubes (CNT)

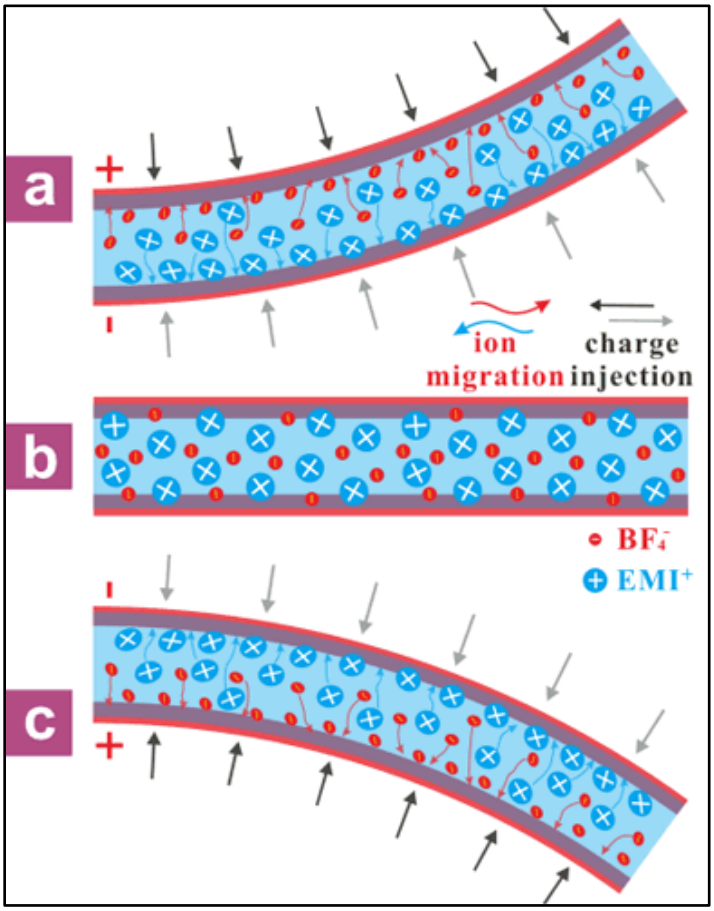

Figure 32: Image of CNT actuator

Carbon nanotube (CNT) actuators were created in 1999 by Ray H. Baughman et al [52]. The carbon bond length is what causes CNT actuation. CNT's are submerged in electrolyte, which allows charges to affect the charge balance between the CNT and electrolyte, as shown in Figure 32. Increasing defection is achieved by increasing the amount of charge. There are two types of CNT's: single walled CNT (SWNT) and multi walled CNT (MWNT). SWNT are made from

graphene layers being wound into tubes. MWNT are made from SWNT that have additional coaxially wrapped graphene tubes.

4.5.1 CNT Model

$$\delta = \delta_b + \delta_s = \frac{FL^3}{192EI} + \frac{f_s FL}{4GA} \tag{4.33}$$

$$I = \frac{\pi D^4}{64} \tag{4.34}$$

$$\sigma^2 = \frac{0.4243 L^3 kT}{Y(a^4 - b^4)} \tag{4.35}$$

The models are from Geoffrey Spinks, Gordon Wallace, Ray Baughman, and Liming Dai [53]. Equation (4.33) applies to SWNT. The total deflection (δ) is the sum of the bending deflection (δ_b) and the shear deflection (δ_s). The bending deflection is a function of force (F), length (L), the elastic modulus (E), second moment of inertia (I); the shear deflection is a function of force, length, shape factor (f_s), shear modulus (G), and cross-section area (A). The moment of inertia is a function of the beams diameter (D). Equation (4.35) applies to MWNT. The mean square amplitude of vibration (σ^2) is a function of length, thermal energy (kT), Young's modulus (Y), outer diameter (a), and inner diameter (b).

Chapter 5: Experimental McKibben Actuators

5.1 Theory

Using the C. Chou and B. Hannaford model gives results for the fiber angle. Taking the derivative of equation (2.1) with respect to fiber angle and setting this equation equal to zero gives the critical points for the force equation. A fiber angle of 0 degrees (parallel with the actuator's longitudinal axis) results in maximum force output of the actuator, and setting the angle to 90 degrees (perpendicular to the actuator's longitudinal axis) results in the minimum force output. Force output can also be improved by increasing actuator diameter, internal pressure, and increasing wall thickness. Girish Krishnan et al investigated the effect of varying the fiber angle of fiber reinforced PAMs [54]. When the force in equation (2.1) is set to zero theta is 54.74°. At this angle the actuator will generate maximum contraction. If θ is greater than 54.74° the actuator will get longer as the internal air pressure is increases while the diameter shrinks; if θ is less than 54.7° the actuator will contract axially as the internal pressure is increased and the diameter will increase.

The problem with the previous models for the McKibben actuator is they don't account for the elastic bladder material. Alternative force models were created by C. Kothera et al. [55] which takes the elastomeric material into account. They derive their models from two different methods: principle of virtual work (5.1) and force balance (5.5). The principle of virtual work model depends on 3 terms: the Gaylord force model ($F_{Gaylord}$), the Mooney-Rivlin model ($F_{cM\text{-}R}$), and a braid effect term (F_{Br}). The variables (C_{10}) and (C_{01}) are elastic material constants chosen from experimental data. In equation (5.5), variable (E_R) is the elastic modulus of the bladder and (V_b) is the volume of the bladder. Kothera et al. found that the model using force balancing

resulted in more accurate force measurements. The force balance method relies on actuator parameters that are readily available, but the virtual work model requires constants that are determined from experimentation.

$$F = F_{Gaylord} - F_{cM-R} - F_{Br} \tag{5.1}$$

$$F_{Gaylord} = \frac{P}{4N^2\pi}\left(3L^2 - B^2\right) \tag{5.2}$$

$$F_{cM-R} = V_b\left\{2C_{10}\left[\lambda_1\frac{d\lambda_1}{dL} + \lambda_2\frac{d\lambda_2}{dL} + \lambda_3\frac{d\lambda_3}{dL}\right] + 2C_{01}\left[\lambda_1\left(\lambda_2^2+\lambda_3^2\right)\frac{d\lambda_1}{dL} + \lambda_2\left(\lambda_3^2+\lambda_1^2\right)\frac{d\lambda_2}{dL} + \lambda_3\left(\lambda_1^2+\lambda_2^2\right)\frac{d\lambda_3}{dL}\right]\right\} \tag{5.3}$$

$$\lambda_1 = \frac{L}{L_0}, \lambda_2 = \frac{R - t/2}{R_0 - t_0/2}, \lambda_3 = \frac{t}{t_0} \tag{5.4}$$

$$F = \frac{P}{4N^2\pi}\left(3L^2 - B^2\right) + P\left(\frac{V_b}{L} - \frac{tL^2}{2\pi RN^2}\right) + E_R V_b\left(\frac{1}{L_0} - \frac{1}{L}\right) + \frac{E_R L}{2\pi RN^2}\left(tL - t_0 L_0\right) \tag{5.5}$$

$$V_b = L\left[\pi R^2 - \pi\left(R-t\right)^2\right] \tag{5.6}$$

C. Chou and B. Hannaford, and G. Klute et al found that the McKibben actuator can behave similarly to biological muscle [5], [56]. The Hill model is used to evaluate biological muscle movement. Equation (5.7) is the Hill model where (F_m.) is the muscle force, ($F_{m,o}$) is the muscle force at rest length, and muscle velocity (V_m). Variable (a) and (b) are constants that are dependent on the type of animal and the type of muscle. Klute et al found that the McKibben actuator could mimic with the exception of muscle velocity. They suggest using a hydraulic damper in parallel with the actuator to improve the actuators muscle velocity.

$$\left[F_m + a\right]\left[V_m + b\right] = \left[F_{m,o} + a\right]b \tag{5.7}$$

5.2 Actuator Fabrication

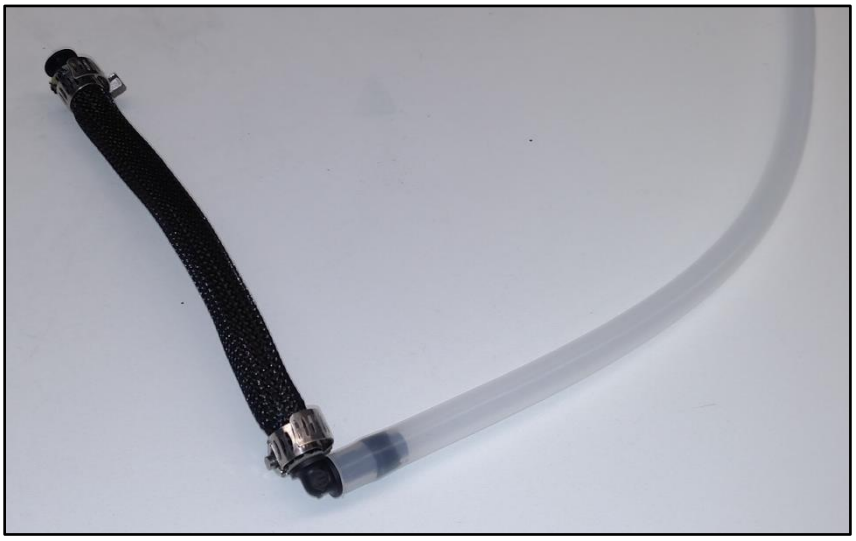

Figure 33: Image of Assembled McKibben Actuator

Figure 34: Image of Updated McKibben Actuator

Silicone tubing was used as the elastic bladder. A 0.25” diameter plug and 0.25” diameter L-shape barbed connectors were used to enclose one end of the tubing and allow air to enter the opposite end. A 0.375” diameter expandable mesh sleeve was attached to the tubing by two metal hose clamps. The mesh sleeve has two fiber angles of equal and opposite angle. Silicone tubing with 0.25” inner diameter was used to connect the open end of the L-shaped barb to an air supply. **Figure 33** is a completed McKibben actuator used for testing. Compressed air was supplied to the open end of the L-

shaped barb. Multiple rubber tubes were used with different harness. Tubes with Shore A Hardness[57] 35, 40, and 50 were used to test how varying hardness affected the actuators performance. The Young's modulus (E) for each hardness can be found using equation (5.8), where (S_A) is the Shore A hardness of the rubber used. The stiffness (k) can be computed using equation (5.9) using the length (L) and cross sectional area (A) of the elastic bladder. The compliance of each hose can be found by taking the inverse of the stiffness.

Table 2 has the Young's modulus, the stiffness, and the compliance values for each tube used for experimentation.

$$E = 10^{(0.0235*S_A - 0.6403)} \tag{5.8}$$

$$k = \frac{EA}{L} \tag{5.9}$$

Each tube had an internal diameter of 0.25" and an outer diameter 0.375". An additional actuator was made using a Shore A 40 hardness tube with an inner diameter of 0.25" and outer diameter of 0.3125". By using softer rubber the actuator should be able to contract greater lengths but at the cost of reduced generated force. Table 1 shows the different types of tubes used for building McKibben actuators. In order to test the McKibben actuator in the MTS machine braided sleeve was placed around the ends the actuator and fastened using the hose clamp in order to make hoops to hold the actuator. Hose clamps needed to be very tight in order to prevent the sleeve sliding out and to minimize air leaks around the barbed connectors. Figure 34 is the image of an updated McKibben actuator. This updated McKibben actuator made it possible to place the actuator inside the MTS machine and test without fear of the actuator slipping out of the clamps. Duct tape was place around the braided sleeve to prevent it from fraying and to better secure the braid to the bladder. Glue was placed between the bladder and the plastic barbs to prevent the bladder from slipping off the barbs.

Table 1: Tubing Used

Durometer (Shore A)	Inner Diameter	Outer Diameter	Material
35 A	0.25”	0.375”	Silicone Rubber
40 A	0.25”	0.375”	Latex Rubber
40 A	0.25”	0.3125”	Latex Rubber
50 A	0.25”	0.375”	Silicone Rubber

Table 2: Calculated Properties of Tubing

Durometer (Shore A)	Young’s Modulus (MPa)	Stiffness (N/m)	Compliance (m/N)
35 A	1.521	418.20	0.00239
40 A (thin)	1.994	246.66	0.00405
40 A	1.994	540.62	0.00185
50 A	3.425	935.15	0.00107

5.3 Control

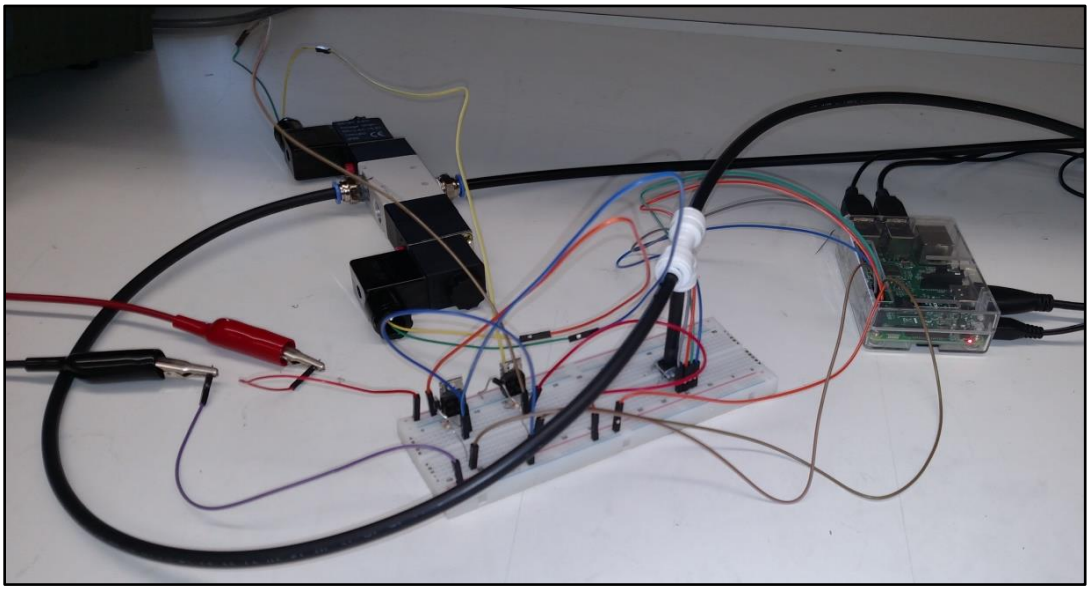

Figure 35: Image of Complete Pneumatic System Setup

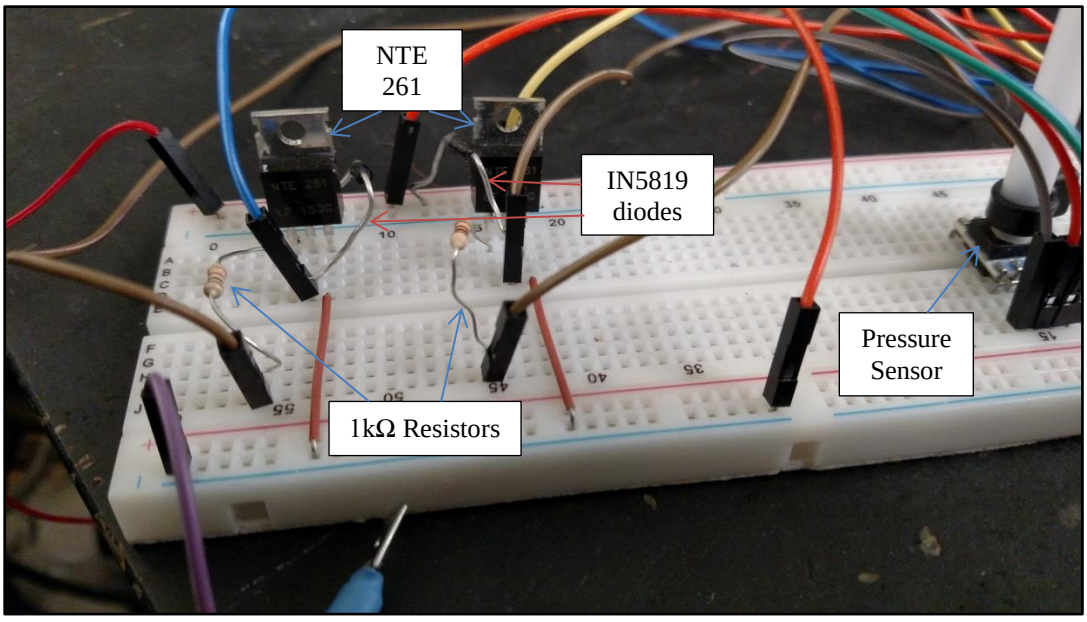

Figure 36: Image of Breadboard Setup

In order to control the actuator for testing a set air pressure had to be applied to an actuator. Figure 35 is the complete setup used to control the actuator. This setup was achieved by using Raspberry Pi 3, 5-port 3-position solenoid air valve (4V230C-08), and a Honeywell board mounted air pressure sensor (SSCDANN150PG2A3). Python 3 was used as the programming language for the Raspberry Pi. A Tektronix CP250 Triple Output Power Supply was used to supply the 12 volts needed to run the solenoid valve. To control the solenoid valve 2-NTE 261transistors, 2-1 kΩ resistors, and 2-IN5819 diodes were used as switches to power the solenoids on and off. The switches were activated using 2 GPIO pins on the raspberry pi: GPIO 17 and GPIO 18. The pressure sensor had to be placed on a breadboard and was connect to the raspberry pi via jumper cables. Figure 36 is an image of the complete breadboard setup.

5.4 Solenoid Valve

Figure 37: Image of (4V230C-08) Solenoid Valve

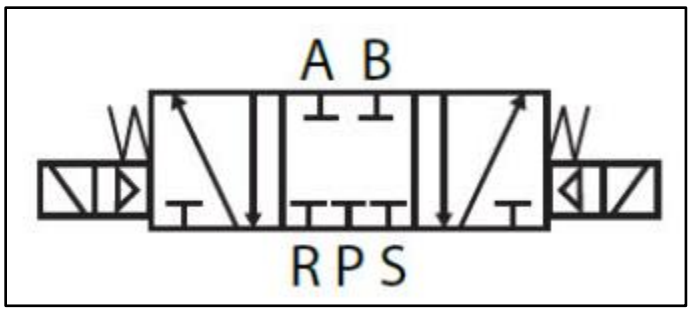

Figure 38: 5/3 Solenoid Valve Schematic

A 5 port, 3 position (5/3) solenoid valve (4V230C-08) was used to control the air going to the McKibben actuator. The image of a 5/3 solenoid valve is shown in Figure 37. Port P is where the air source goes, ports A and B are input ports, and ports R and S are exhaust ports. This solenoid valve is also referred to as a double solenoid because it has two solenoids. This solenoid valve required 12 DC volts to run which was supplied via a Tektronix power supply; this valve had a pressure range of 20-116 psi. The three positions are shown in Figure 38. The center position is when both solenoids are turned off and all five ports are closed. The left position corresponds to when only the left solenoid is turned on, this allows for air to flow from port P to port A while port B is allowed to vent through port S. the right position (right solenoid turned on) is the opposite of the left position, air allowed to flow from port P to port B while port A can vent through port R. This setup allows the actuator to vent the air inside the system and refill the actuator to a different air pressure. Two transistors were used as a switch to power the solenoid valves. By using this solenoid valve controlling the air to actuator was achieved but next a pressure sensor had to be added in order to read the internal air pressure inside the actuator.

5.5 Pressure Sensor

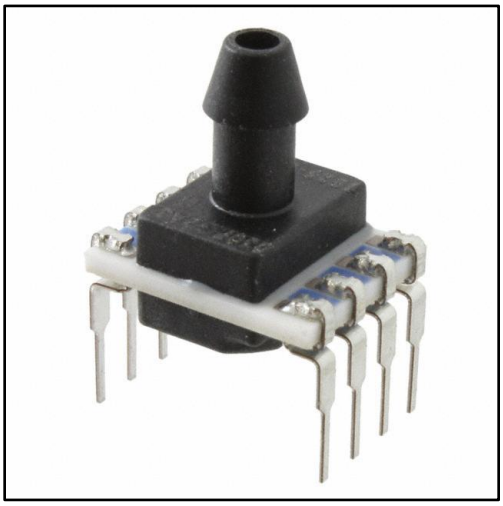

Figure 39: Honeywell (SSCDANN150PG2A3) Pressure Sensor

A Honeywell SSCDANN150PG2A3 board mount pressure was used to measure the air pressure inside the actuator. Figure 39 is the image of the pressure sensor used. This sensor measures gauge pressure using two ports: one with a barbed fitting so an air tube can be attached and the other open to measure the pressure in the room (ambient pressure). The pressure reading is the difference between these two values. The sensor has a ±2% error band for the pressure reading. This sensor is plugged into the breadboard and connected directly to the 3.3 volt, ground, SCL, and SDA pins. When sensor is powered on it gives to bytes of data. From those two bytes of data an output is generated using equation (5.10) and then equation (5.11) is used to determine the internal air pressure. The minimum and maximum outputs are calibration values defined by the manufacturer. These numbers are found on the datasheet using the model number of the sensor. The minimum and maximum pressures are the pressure range specified by the manufacture. Table 3 has the values used for both the pressures and the outputs.

$$output = (byte\_1) * 256 + (byte\_2) \tag{5.10}$$

$$pressure = \frac{(output - output_{\min}) * (pressure_{\max} - pressure_{\min})}{(output_{\max} - output_{\min})} + pressure_{\min} \qquad (5.11)$$

Table 3: Pressure Sensor Variables and Values

Pressure Sensor Variables	Values
$output_{min}$ (10% output)	1638
$output_{max}$ (90% output)	14746
$pressure_{min}$	0 psi
$pressure_{max}$	150 psi

5.6 Raspberry Pi

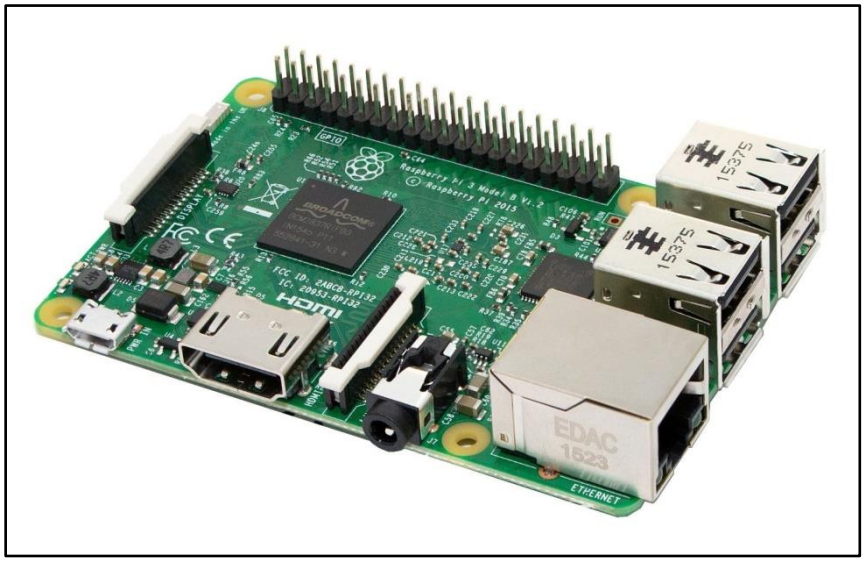

Figure 40: Image of Raspberry Pi 3

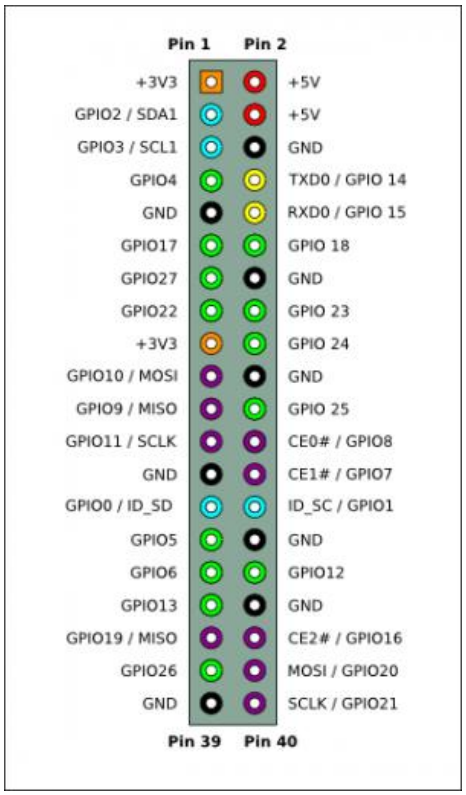

Figure 41: Raspberry Pi 3 pin layout

The Raspberry Pi 3, shown in Figure 40, was the computer used to control the actuator. This was done by opening and closing ports on the solenoid valve when the desired pressure was read by the pressure sensor. The Raspberry Pi 3 has 40 pins with 3.3 volt pins, 5 volt pins, ground pins, and General Purpose Input Output (GPIO) pins. Figure 41 is a diagram of the pin layout for the Raspberry Pi 3. Since this is a computer an external monitor had to be connected via an HDMI cable; an external mouse and keyboard also had to be plugged into the Pi's USB ports. Jumper cables were used to connect the pins to a solderless bread board. Python 3 was used as the programming language to use the pressure sensor and solenoid valve.

5.7 Python Code

The python code controlled the GPIO pins on the raspberry pi. By turning the GPIO pins on and off the solenoid would switch between its three positions. The whole time the code runs the pressure sensor remains on to continuously read the air pressure within the system. The user defines a desired air pressure and when the code is started air is allowed to enter the actuator. Once the desired pressure is met the solenoid is turned off locking the all the ports. The pressure inside the actuator is held for a set time and after that the actuator is allowed exhaust and the procedure is repeated for 10 psi higher air pressure. Once the highest desired pressure is reached the user can terminate the code by pressing the Ctrl+C keys on the keyboard plugged into the Raspberry Pi.

5.8 Air System

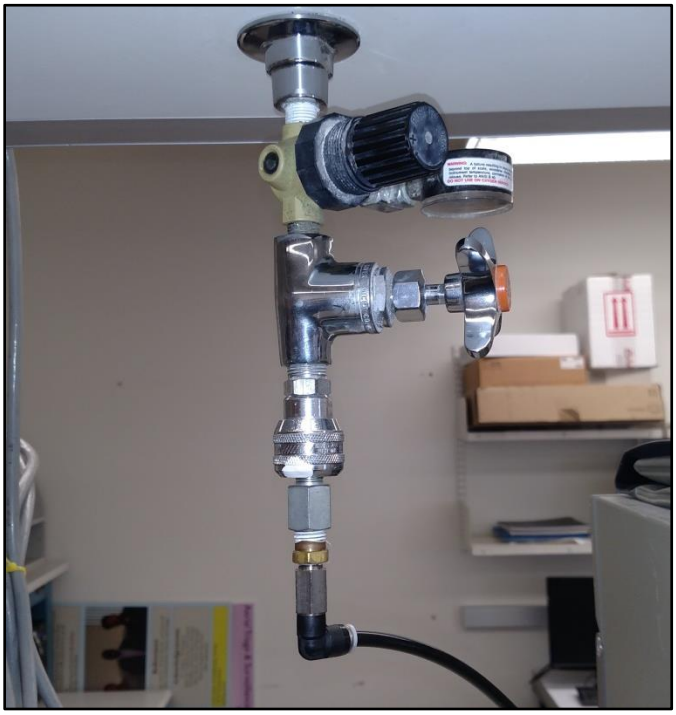

Figure 42: Image of Building Air Compressor

The air system is the method of how the compressed air goes from the air compressor to the pressure sensor and actuator. 0.25” and 0.375” outer diameter hoses were used to transport air. Air first went from the room air compressor, shown in Figure 42, to the air supply port (P) of the solenoid valve. 0 psi to 100 psi could be supplied from the air compressor by turning the regulator dial; the flow of air could also be controlled by turning the handle of the valve. This allowed control of not only the air pressure but also the flow rate. From the solenoid valve air went to one end of a T-coupler. The other ends of the T-coupler are connected to the barbed port of the pressure sensor and the McKibben actuator. In order to connect the McKibben actuator a 0.25” to 0.375” adapter was needed in order to fit the open end of the L-shaped barbed connector to the T-coupler.

5.9 Tensile Testing Machine

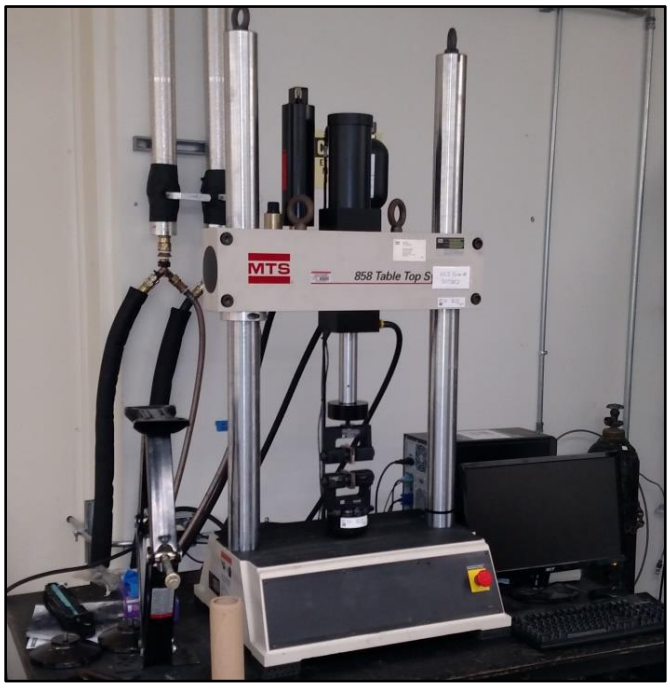

Figure 43: Image of Tensile Testing machine used for testing

A tensile testing machine (858 Tabletop MTS), shown in Figure 43, was used to test the McKibben actuators. This unit has an external hydraulic power unit used to control the pneumatic cylinders of the MTS and a Coolflow system 2 cool box to keep the temperature of the unit optimal. To control the power unit and the MTS machine a desktop computer was connected to these units. GhostWall software was used for the measurements from the MTS.

5.10 Testing

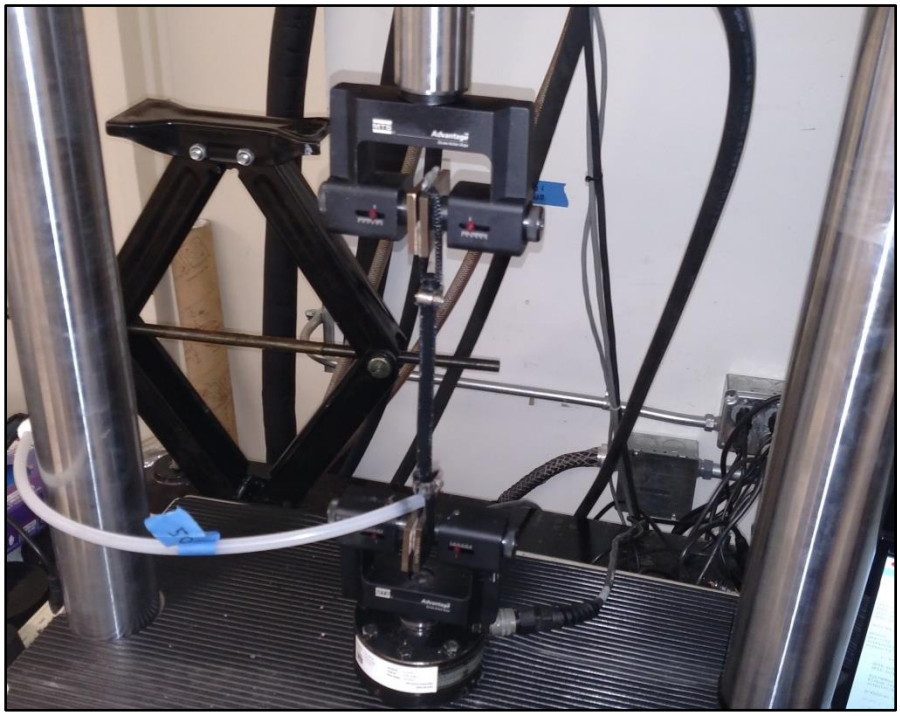

Figure 44: Actuator Test Setup for Exerted Force

Testing focused on measuring the force generated by the actuator at certain air pressures. Each actuator was placed in the clamps of the MTS machine and held at a constant distance. Force measurements were taken as the pressure inside the actuator was increased by 10 psi until a max pressure of 100 psi was reached. Air pressure was slowly turned up to get the most accurate

pressure readings. Figure 44 is the image of one of the McKibben actuators being tested. Force was measured in newtons.

5.11 Results

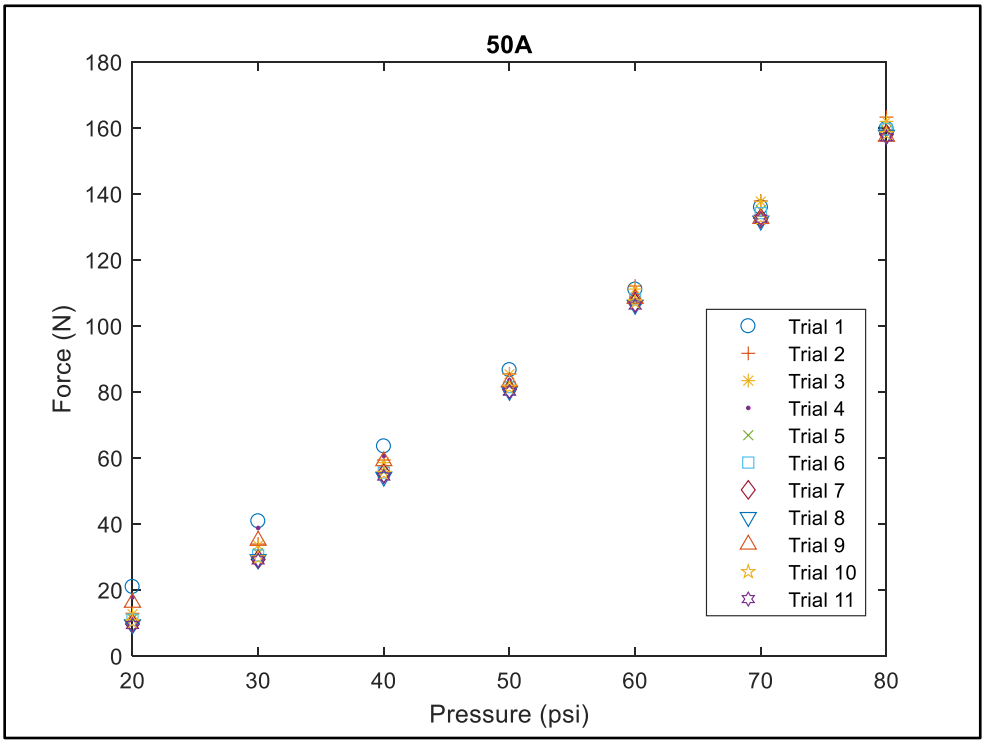

Figure 45: Force vs Pressure (50A)

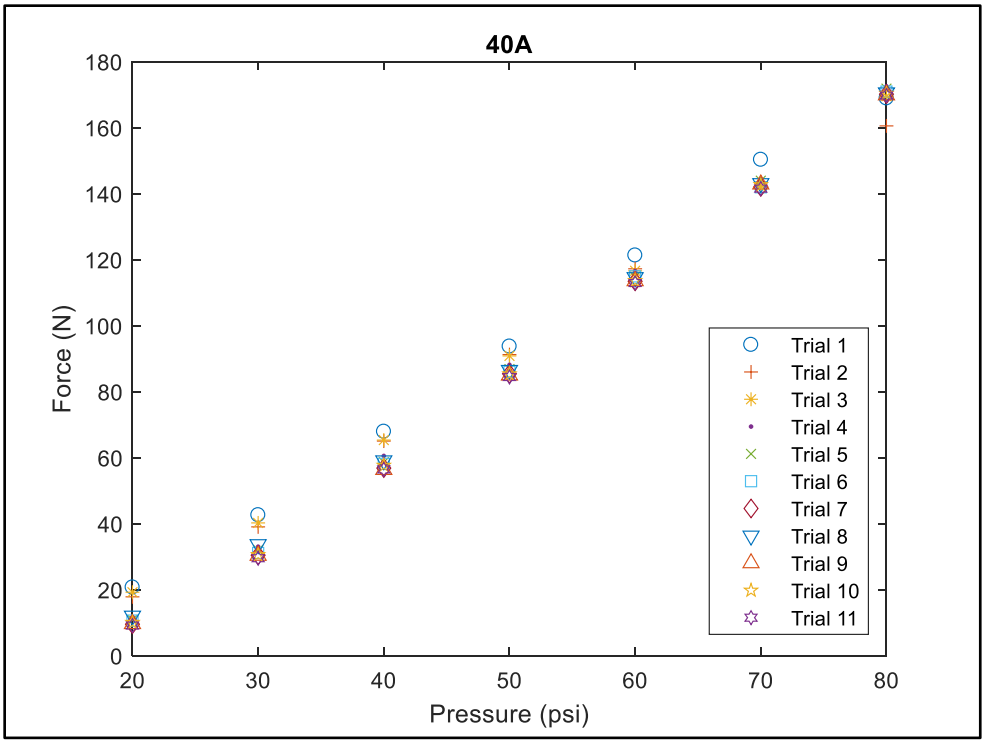

Figure 46: Force vs Pressure (40A)

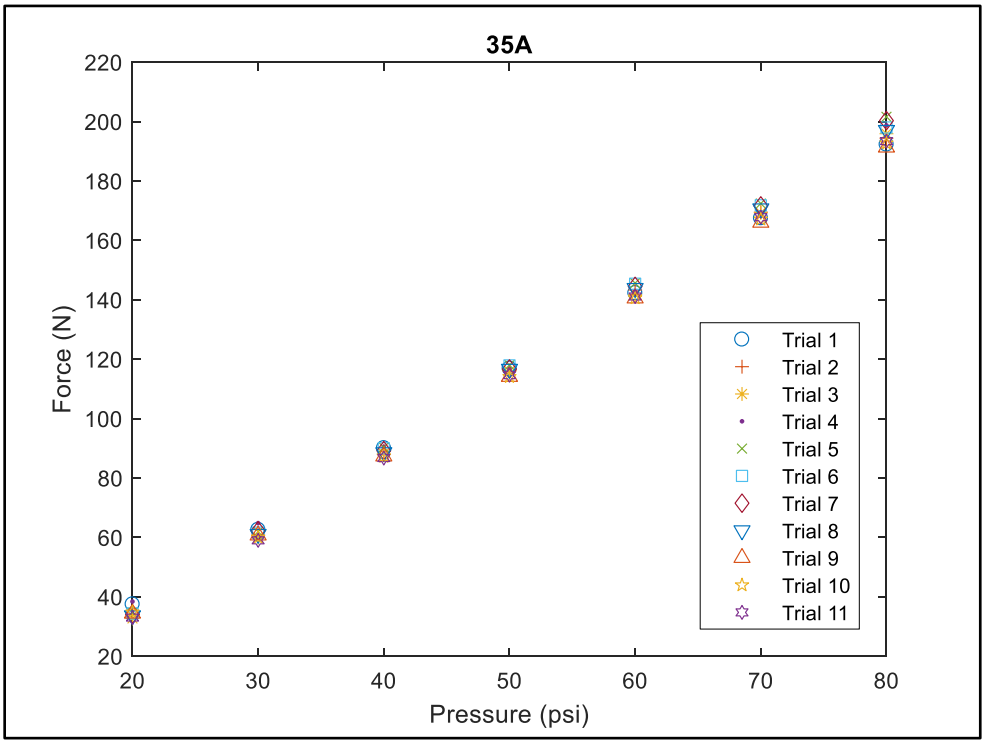

Figure 47: Force v Pressure (35A)

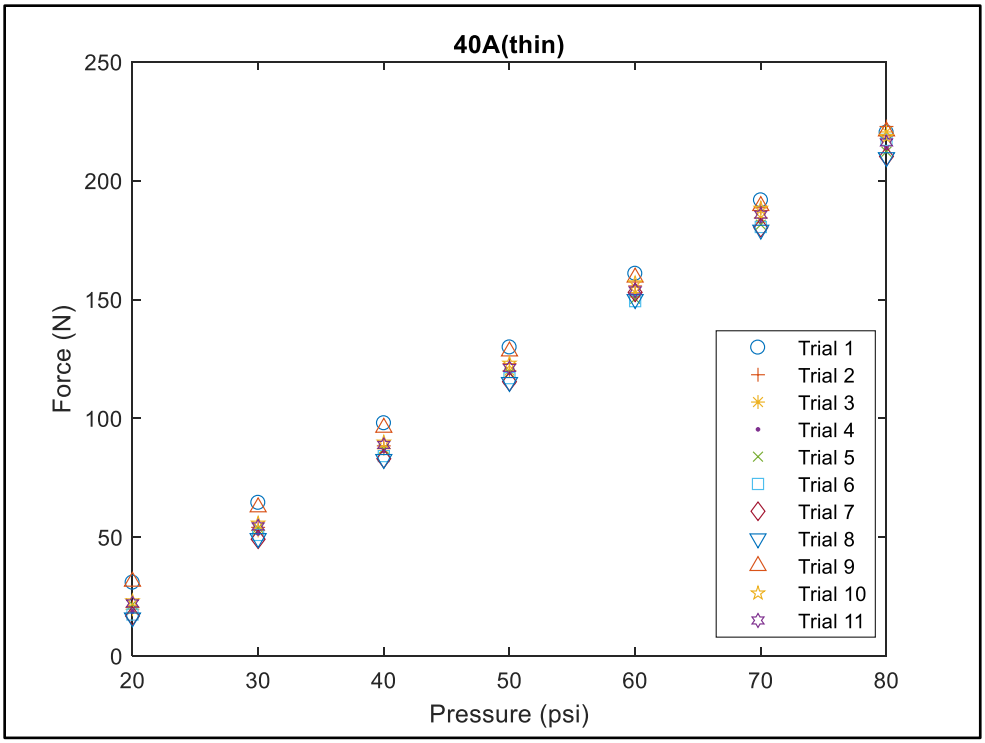

Figure 48: Force vs Pressure (40A thin)

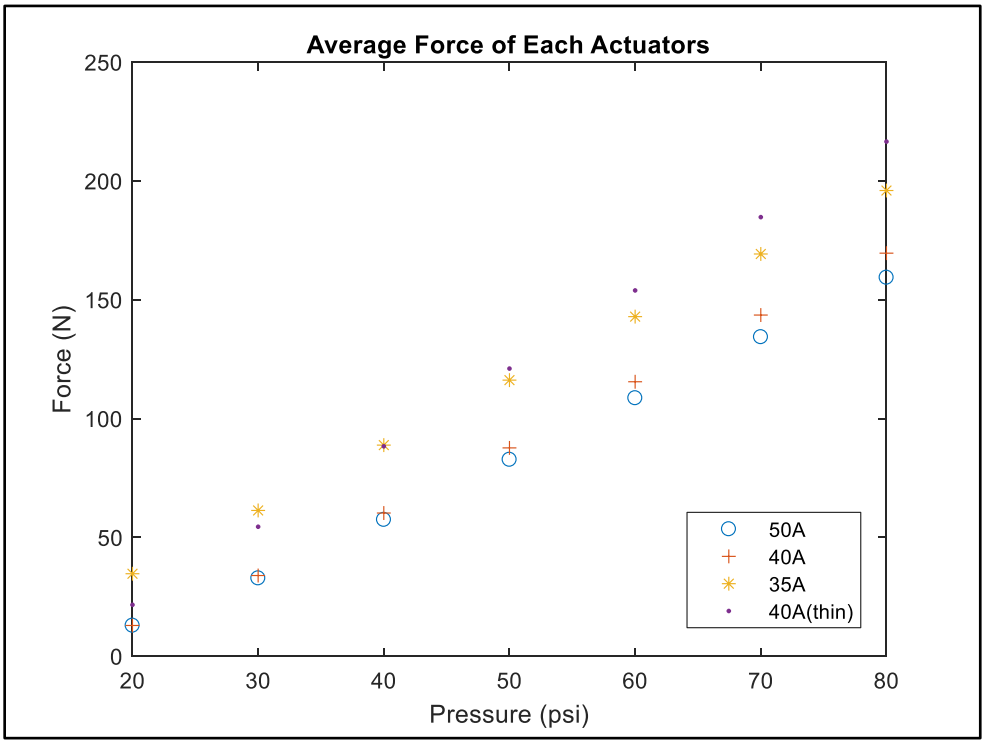

Figure 49: Force vs Pressure (all)

Figure 45-Figure 48 shows the trials for each actuator. Each trial consisted of subjecting the actuator to internal air pressures from 20 to 80 psi, in 10 degree increments. Eleven trials were recorded for each actuator over the course of 2-3 days. The bladders made of latex rubber saw a larger drop in generated force after the first few trials while the silicone bladders generated force remained consistent throughout all the trials. This explains the lower force output of the thin 40A actuator compared to the 35A actuator for air pressures 20 and 30 psi. Out of the 4 actuators the 35A silicone rubber was the most resilient; it produced the most consistent force readings at each air pressure.

Figure 49 **shows the force generated from each actuator. This plot was generated by taking the average of the trials for each actuator (Figure 45-Figure 48). The thin wall tube with 40A hardness exerted the highest force while the hardest elastic bladder (50A) generated the smallest amount of force. This is due to the wider gap between the elastic bladder and the mesh sleeve, which allowed this actuator to radially expand more. The harder rubber and narrower gap between the bladder and sleeve prevented the actuator from contracting. The results also correspond to the stiffness of the tube (**

Table 2). The tube with the lowest stiffness exerted the higher force while the the tubes with higher stiffness exerted less force. Figure 49 also shows that there is little dependence on material selection, with latex rubber only performing slightly better than the silicone rubber.

5.12 Force Comparison with Theoretical Model

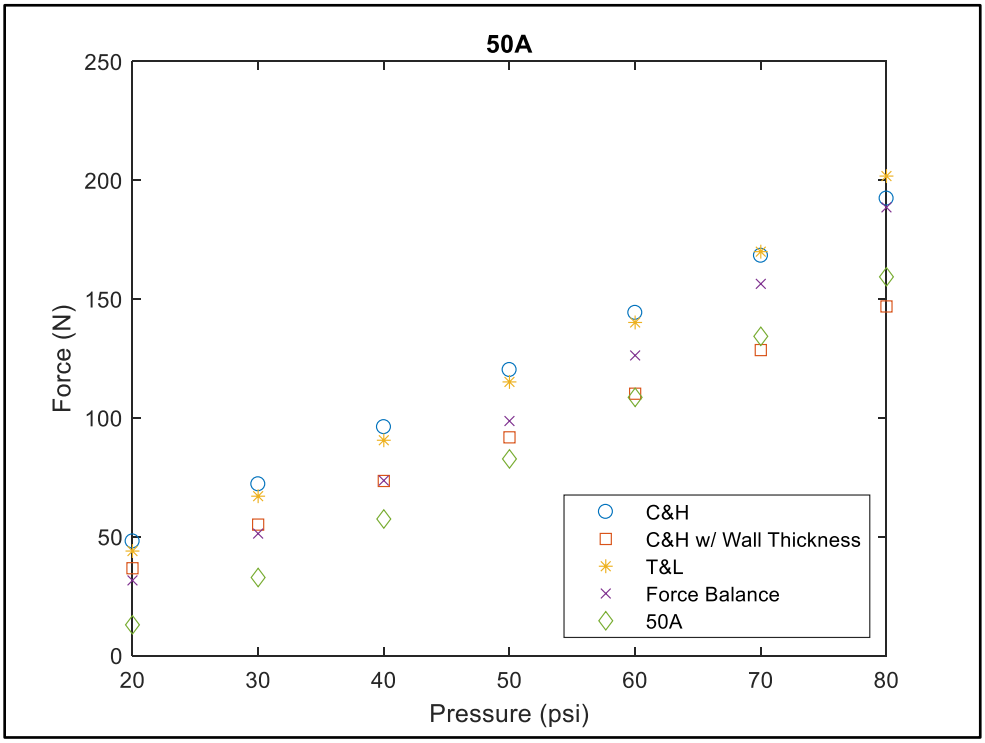

Figure 50: Force vs Pressure (50A)

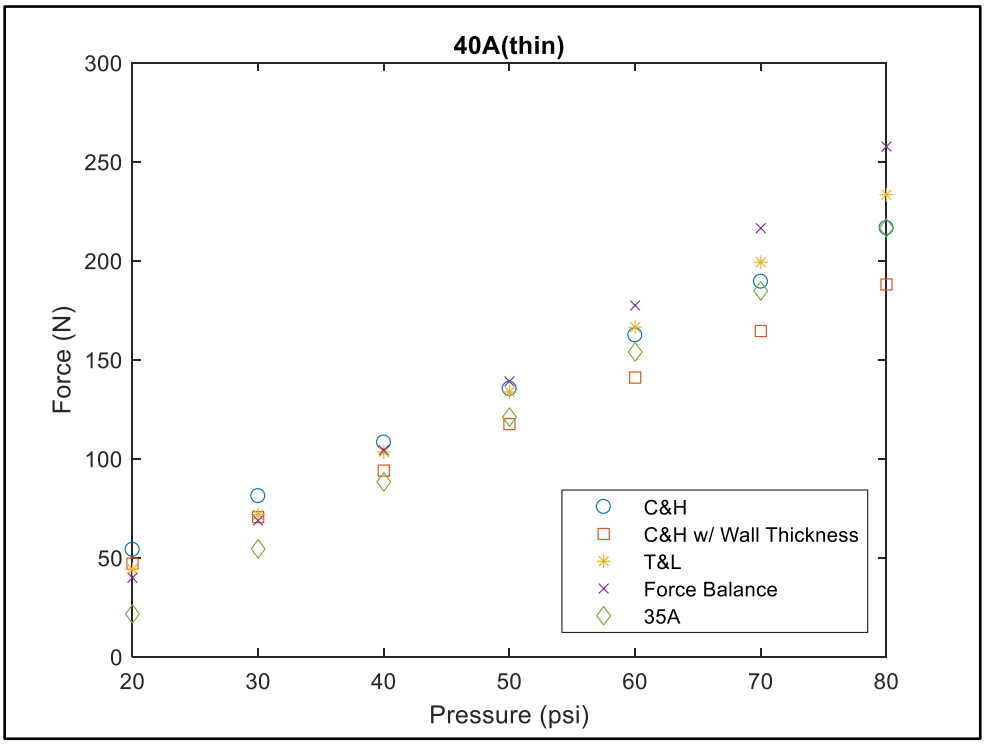

Figure 51: Force vs Pressure (40A thin)

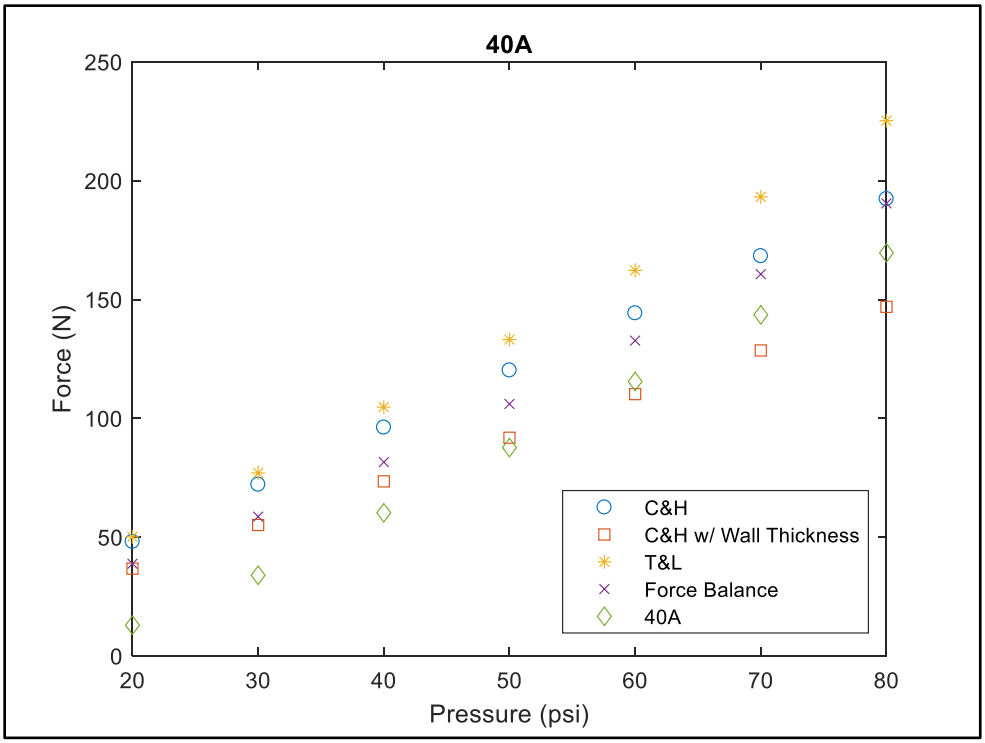

Figure 52: Force vs Pressure (40A)

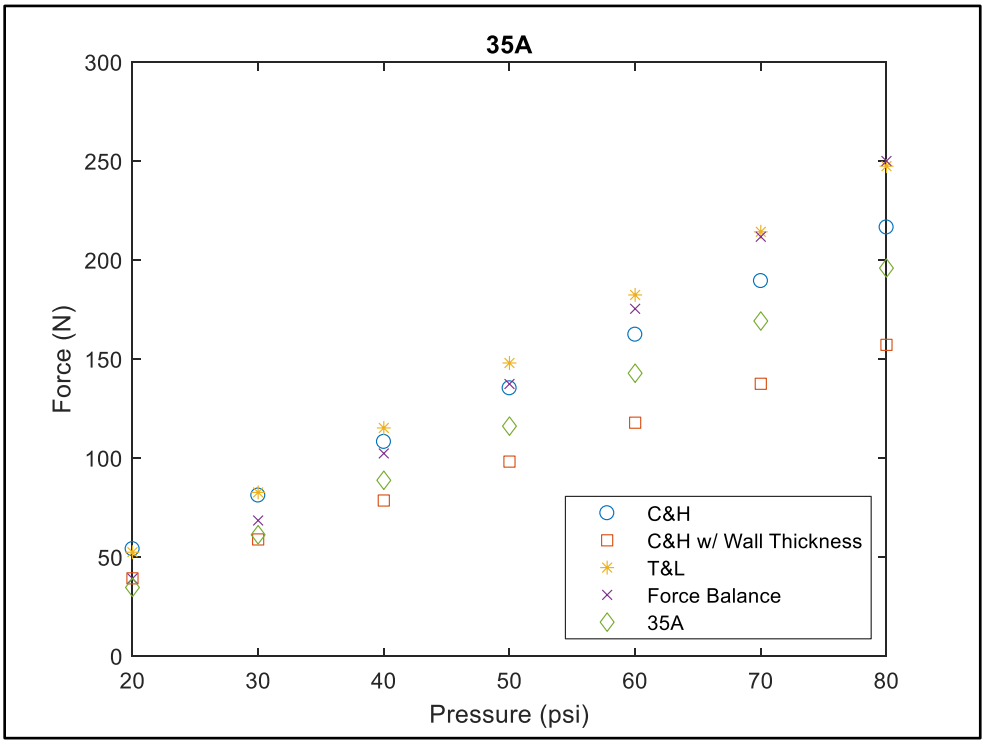

Figure 53: Force vs Pressure (35A)

Figure 50-Figure 53 are the force plots of each actuator in comparison with theoretical models. Three theoretical models were used to evaluate the actuators: the model by C. Chou and B. Hannaford model, the model by B. Tondu and P. Lopez, and the force balance model. There is no clear best model due to the different constants and material parameters needed for evaluation. The Chou and Hannaford model accounting for the thickness of the elastic bladder is a preferred model because it depends only on values that don't require the actuator to be tested. The other models require values that have to be tested for experimentally.

5.13 Applications

The McKibben actuator has many applications including aerospace, biomedical, and industrial. They generate a decent amount of force for their light weight and can be used in place of some pneumatic cylinders. These actuators are also small so they can fit in small, confined spaces. G. Andrikopoulos, G. Nikolakopoulos and S. Manesis conducted a survey on the applications of not only McKibben actuators but also other PAMs [1]. The following are examples of some McKibben actuator applications.

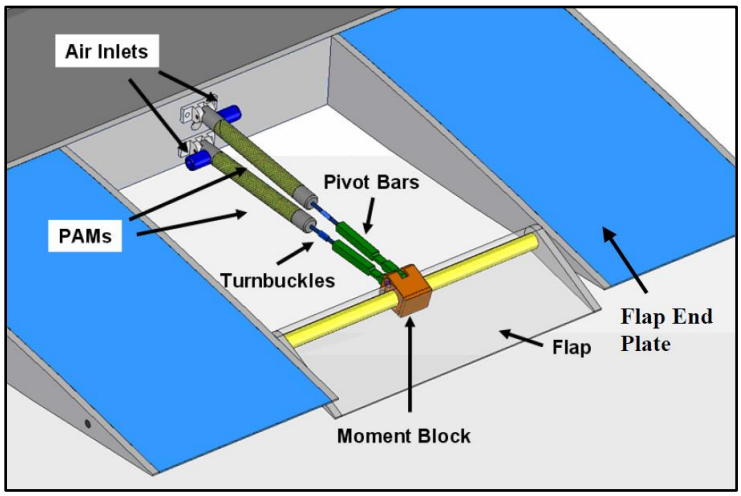

Figure 54: Model of PAM Trailing Edge Flap [58]

Figure 55: Image of Morphing Cell for Wing [59]

Benjamin K.S. Woods et al created an airfoil that utilizes McKibben actuators (Figure 54) to move a trailing edge flap [58]. Two actuators are used in an antagonistic setup to adjust the angle of the flap. The flap was capable of being deflected about 20 degrees. N. Wereley et al also tested PAMs for aerospace applications[59], [60]. They demonstrated that in addition to using McKibben actuators for trailing edge flaps they can also be used for a morphing cell for a wing (Figure 55). The morphing cell consisted of an X-shaped frame and two McKibben actuators. The actuators are used to control the shape of the X frame. The idea behind the morphing cell is to increase the wing span and area of the air craft which increases the aspect ratio of the wing. Increasing the wings aspect ratio increases parasite drag but reduces induced drag of an aircraft and vice versa for decreasing the wings aspect ratio.

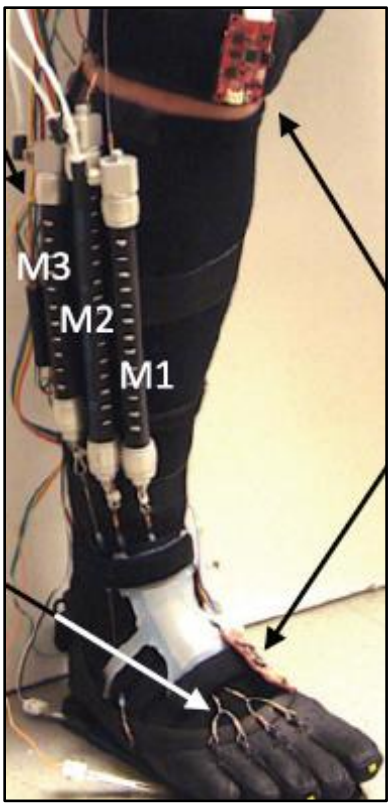

Figure 56: Image of Ankle-foot Rehabilitation device [61]

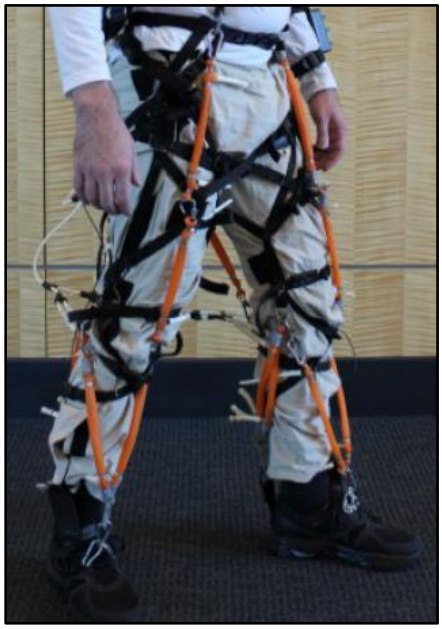

Figure 57: Image of Soft Exosuit [62]

Assistive and rehabilitation devices are the main biomedical applications for the McKibben actuator. An ankle-foot rehabilitation device (Figure 56) and a soft exosuit were created using McKibben actuators. The ankle-foot robotic device was created by Yong-Lae Park et al [61] and a soft exosuit (Figure 57) was created by Michael Wehner et al [62]. The ankle-foot robotic device is worn around a user's foot and ankle. It uses four McKibben actuators to assist the user lift their foot. Certain neuromuscular conditions can limit a person's ability to lift there foot up. This device would aid in lifting the user's foot preventing potential falls. This device could also be used as a rehabilitation device to help users regain mobility and function in their ankle and foot. The soft exosuit is a device that is worn over a user's legs and assists in leg movement. It is not meant to be rehabilitation device but a device to reduce the power used for walking. This is achieved by using specifically placed McKibben actuators that when actuated assist leg movement. The main advantages using McKibben actuators are they are light weight and capable of exerting forces equal or greater to human muscle.

Figure 58: Image of Fluidic Muscle Motion Seat [63]

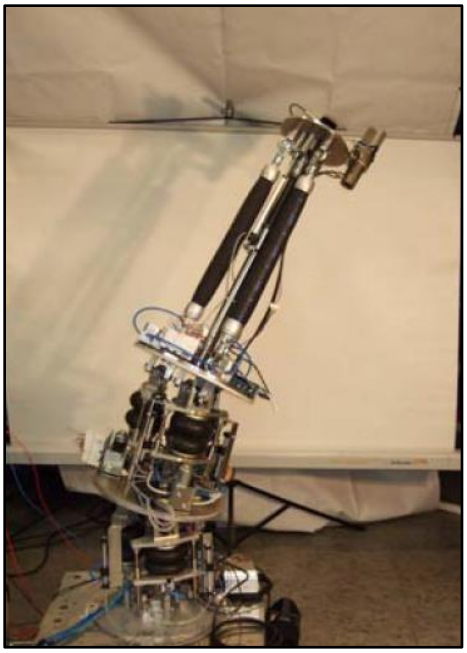

Figure 59: Image of Modular Hybrid Robot [64]

McKibben actuators have multiple industrial applications. M. Pohl developed a motion seat called the “Fluidic Muscle (FM) Motion Seat” (Figure 58) that can be used for as a flight or driving simulator [63]. The seat is attached to a frame using 6 fluidic actuators. The use of 6 actuators gives the seat six degrees of freedom. A modular robotic hybrid manipulator (Figure 59) was created by J. Radojicic, D. Surdilovic, and G. Schreck [64]. This manipulator has a modular design with each module containing either bellow actuator or Fluidic actuators, and is safe for human interaction. Each module needs at least three bellow or three fluidic actuators for stability. Modules can be stacked in order to make more complex movements. This manipulator is very similar to the OCTARM manipulator from section 2.11. The manipulator is controlled by changing the air pressure in each individual actuator. Applications of this manipulator include assembly lines and grasping tasks. The size of the manipulator can be changed by adjusting the size of the actuators used.

There are many diverse applications for McKibben actuators. As improvements to McKibben actuators are made the number of applications will increase. For many applications McKibben actuators are ideal because they are light weight, can produce significant forces, and are inexpensive to produce.

Chapter 6: Conclusion

6.1 Conclusion

Soft robotics is a promising technology that will allow robots to have more capabilities than conventional hard robots. Hard robots consist of rigid, hard links while soft robots utilize materials that are soft, light, and compliant. Soft robots can be controlled using fluid and/or an applied electric field. These actuators can create linear, twist, or bend movement when actuated. Soft robots allow for greater flexibility and more complex movements than hard robots.

Some of the advantages of soft robots are their ability to replicate natural biological movements and lighter weight due to use of lighter, softer materials. Since soft robots can mimic natural biological movement that makes them suitable for applications involving people and animals. Soft robots don't require the use of multiple motors like hard robots. Soft robots don't use hard, rigid joints, which allow them to be flexible and compliant.

Drawbacks of soft robotics include limited modeling due to nearly infinite degrees of freedom and limited force output compared to hard robots. Soft robots are more difficult to fabricate due to the different materials and techniques needed for manufacturing. One solution to the limited capabilities of soft robotics is to combine them with hard robotics. Combining these two robots can reduce some of the limitations of hard and soft robots. G. Whitesides et al created a hard/soft robot by using an iRobot and connecting a PneuNet gripper to it [65]. The iRobot is driven near an object and the PneuNet is used to go and grab the object, then the iRobot is driven back to its original location. The hard robot and soft robot are controlled using a joystick. This robot is ideal for search and rescue missions as well as other retrieval based tasks.

Future research should focus on better understanding of soft robotic properties and modeling. The modeling could lead to a general theory for modeling these types of systems focused on continuous systems modeling. Work also has to be done on how to integrate soft robots in order to replace or collaborate with hard robots. New compliant materials are needed to optimize these soft robotic actuators. As research and development for soft robotics continues to grow, the number of applications and uses will also increase. Soft robotics is an alternative approach to robotics that has many benefits and an infinite amount of applications.

6.2 Works Cited

[1] G. Andrikopoulos, G. Nikolakopoulos, and S. Manesis, "A Survey on applications of Pneumatic Artificial Muscles," in *2011 19th Mediterranean Conference on Control Automation (MED)*, 2011, pp. 1439–1446.

[2] K. J. Kim and S. Tadokoro, Eds., *Electroactive polymers for robotic applications: artificial muscles and sensors*. London: Springer, 2007.

[3] F. Daerden and D. Lefeber, "Pneumatic artificial muscles: actuators for robotics and automation," *Eur. J. Mech. Environ. Eng.*, vol. 47, no. 1, pp. 11–21, 2002.

[4] A. H. Morin, "US2642091.pdf." [Online]. Available: https://docs.google.com/viewer?url=patentimages.storage.googleapis.com/pdfs/US2642091.pdf. [Accessed: 04-Nov-2016].

[5] C.-P. Chou and B. Hannaford, "Measurement and modeling of McKibben pneumatic artificial muscles," *IEEE Trans. Robot. Autom.*, vol. 12, no. 1, pp. 90–102, 1996.

[6] H. Schulte Jr., *The Characteriastics of the McKibben Artificial Muscle*. National Aceademy of Sciences-National Research Council, 1961.

[7] B. Tondu and P. Lopez, "Modeling and control of McKibben artificial muscle robot actuators," *IEEE Control Syst.*, vol. 20, no. 2, pp. 15–38, Apr. 2000.

[8] P. J. D. C, "Bellows actuator," US3319532 A, 16-May-1967.

[9] G. Immega, "Bellows actuator," US5181452 A, 26-Jan-1993.

[10] Y. J. M, "Fluid actuator," US3645173 A, 29-Feb-1972.

[11] G. Immega and M. Kukolj, "Axially contractable actuator," US4939982 A, 10-Jul-1990.

[12] H. M. Paynter, "High pressure fluid-driven tension actuators and method for constructing them," US4751869 A, 21-Jun-1988.

[13] H. M. Paynter, "Hyperboloid of revolution fluid-driven tension actuators and method of making," US4721030 A, 26-Jan-1988.

[14] M. Kukolj, "Axially contractable actuator," US4733603 A, 29-Mar-1988.

[15] K. Suzumori, S. Iikura, and H. Tanaka, "Flexible microactuator for miniature robots," in *IEEE Micro Electro Mechanical Systems, 1991, MEMS '91, Proceedings. An Investigation of Micro Structures, Sensors, Actuators, Machines and Robots*, 1991, pp. 204–209.

[16] F. Daerden, "Conception and realization of pleated pneumatic artificial muscles and their use as compliant actuation elements," *Vrije Univ. Brussel Belg.*, 1999.

[17] "Soft Robotics Toolkit." [Online]. Available: http://softroboticstoolkit.com/home. [Accessed: 29-Sep-2016].

[18] M. B. Pritts and C. D. Rahn, "Design of an artificial muscle continuum robot," in *2004 IEEE International Conference on Robotics and Automation, 2004. Proceedings. ICRA '04*, 2004, vol. 5, p. 4742–4746 Vol.5.

[19] I. D. Walker *et al.*, "Continuum robot arms inspired by cephalopods," 2005, p. 303.

[20] T. Ranzani, M. Cianchetti, G. Gerboni, I. De Falco, G. Petroni, and A. Menciassi, "A modular soft manipulator with variable stiffness," in *3rd joint workshop on new technologies for computer/robot assisted surgery*, 2013, pp. 11–13.

[21] F. Ilievski, A. D. Mazzeo, R. F. Shepherd, X. Chen, and G. M. Whitesides, "Soft Robotics for Chemists," *Angew. Chem.*, vol. 123, no. 8, pp. 1930–1935, Feb. 2011.

[22] R. F. Shepherd *et al.*, "Multigait soft robot," *Proc. Natl. Acad. Sci.*, vol. 108, no. 51, pp. 20400–20403, 2011.

[23] M. T. Tolley *et al.*, “A Resilient, Untethered Soft Robot,” *Soft Robot.*, vol. 1, no. 3, pp. 213–223, Sep. 2014.
[24] P. Polygerinos *et al.*, “Towards a soft pneumatic glove for hand rehabilitation,” in *2013 IEEE/RSJ International Conference on Intelligent Robots and Systems*, 2013, pp. 1512–1517.
[25] B. Mosadegh *et al.*, “Pneumatic Networks for Soft Robotics that Actuate Rapidly,” *Adv. Funct. Mater.*, vol. 24, no. 15, pp. 2163–2170, Apr. 2014.
[26] B. Mosadegh *et al.*, “Supplemental Information.”
[27] F. Connolly, C. J. Walsh, and K. Bertoldi, “Automatic design of fiber-reinforced soft actuators for trajectory matching,” *Proc. Natl. Acad. Sci.*, p. 201615140, Dec. 2016.
[28] J. Bishop-Moser, G. Krishnan, and S. Kota, “Fiber-reinforced actuator,” US20150040753 A1, 12-Feb-2015.
[29] F. Connolly, P. Polygerinos, C. J. Walsh, and K. Bertoldi, “Mechanical Programming of Soft Actuators by Varying Fiber Angle,” *Soft Robot.*, vol. 2, no. 1, pp. 26–32, Mar. 2015.
[30] C. Keplinger, M. Kaltenbrunner, N. Arnold, and S. Bauer, “Rontgen’s electrode-free elastomer actuators without electromechanical pull-in instability,” *Proc. Natl. Acad. Sci.*, vol. 107, no. 10, pp. 4505–4510, Mar. 2010.
[31] F. Carpi and D. De Rossi, “Dielectric elastomer cylindrical actuators: electromechanical modelling and experimental evaluation,” *Mater. Sci. Eng. C*, vol. 24, no. 4, pp. 555–562, Jun. 2004.
[32] F. Carpi, C. Salaris, and D. D. Rossi, “Folded dielectric elastomer actuators,” *Smart Mater. Struct.*, vol. 16, no. 2, pp. S300–S305, Apr. 2007.
[33] Y. Bar-Cohen, Society of Photo-optical Instrumentation Engineers, Society for Experimental Mechanics (U.S.), U.S. Air Force Wright Laboratory, Nihon Seramikkusu Kyōkai, and Intelligent Materials Forum (Mitō Kagaku Gijutsu Kyōkai), Eds., *Smart structures and materials 1999. 1-2 March 1999, Newport Beach, California /. Electroactive polymer actuators and devices*. Bellingham, Wash., USA: SPIE, 1999.
[34] I. C. S. S. E. S. Committee and I.-S. S. Board, “Ieee recommended practice for software requirements specifications,” 1988.
[35] A. Katchalsky, W. Kuhn, B. Hargitay, and A. Eisenberg, “Reversible Dilation and Contraction by Changing the State of Ionization of High-Polymer Acid Networks,” 1950. [Online]. Available: http://www.nature.com/nature/journal/v165/n4196/pdf/165514a0.pdf. [Accessed: 06-Nov-2016].
[36] T. Shiga, “Deformation and viscoelastic behavior of polymer gels in electric fields,” in *Neutron spin echo spectroscopy viscoelasticity rheology*, Springer, 1997, pp. 131–163.
[37] H. Finkelmann, H.-J. Kock, and G. Rehage, “Investigations on liquid crystalline polysiloxanes 3. Liquid crystalline elastomers — a new type of liquid crystalline material,” *Makromol. Chem. Rapid Commun.*, vol. 2, no. 4, pp. 317–322, Jun. 1981.
[38] B. R. Ratna, D. L. Thomsen III, and P. Keller, “Liquid crystall elastomers as artificial muscles: role of side-chain-backbone coupling,” 2001, vol. 4329, pp. 233–237.
[39] D. L. Thomsen *et al.*, “Liquid Crystal Elastomers with Mechanical Properties of a Muscle,” *Macromolecules*, vol. 34, no. 17, pp. 5868–5875, Aug. 2001.
[40] H. Wermter and H. Finkelmann, “Liquid crystalline elastomers as artificial muscles,” *E-Polym.*, vol. 1, no. 1, pp. 111–123, 2001.
[41] H. Finkelmann, E. Nishikawa, G. G. Pereira, and M. Warner, “A New Opto-Mechanical Effect in Solids,” *Phys. Rev. Lett.*, vol. 87, no. 1, Jun. 2001.

[42] W. Lehmann *et al.*, “Direct and inverse electromechanical effect in ferroelectric liquid crystalline elastomers,” *J. Appl. Phys.*, vol. 86, no. 3, p. 1647, 1999.
[43] Y. Bar-Cohen, “EAP history, current status, and infrastructure,” *Electroact. Polym. EAP Actuators Artif. Muscles*, pp. 3–44, 2001.
[44] J. Su, T. L. St. Clair, Y. Bar-Cohen, and S. Leary, “Electrostrictive Graft Elastomers and Applications,” 1999. [Online]. Available: https://ntrs.nasa.gov/archive/nasa/casi.ntrs.nasa.gov/20000055583.pdf. [Accessed: 06-Nov-2016].
[45] J. Kim, J.-Y. Kim, and S. Choe, “Electroactive papers: possibility as actuators,” 2000, vol. 3987, pp. 203–209.
[46] G. Inzelt, *Conducting Polymers*. Berlin, Heidelberg: Springer Berlin Heidelberg, 2008.
[47] F. Carpi, Ed., *Electromechanically Active Polymers*. Cham: Springer International Publishing, 2016.
[48] I. Chopra and J. Sirohi, *Smart structures theory*, First edition. New York, NY, USA: Cambridge University Press, 2014.
[49] J. P. Gong, T. Nitta, and Y. Osada, “Electrokinetic modeling of the contractile phenomena of polyelectrolyte gels. One-dimensional capillary model,” *J. Phys. Chem.*, vol. 98, no. 38, pp. 9583–9587, 1994.
[50] A. Katchalsky, “Rapid swelling and deswelling of reversible gels of polymeric acids by ionization,” *Cell. Mol. Life Sci.*, vol. 5, no. 8, pp. 319–320, 1949.
[51] S. Nemat-Nasser and J. Y. Li, “Electromechanical response of ionic polymer-metal composites,” *J. Appl. Phys.*, vol. 87, no. 7, pp. 3321–3331, 2000.
[52] M. Kertesz, “Ray H. Baughman,* Changxing Cui, Anvar A. Zakhidov, Zafar Iqbal, Joseph N. Barisci, 2 Geoff M. Spinks, 2 Gordon G. Wallace, 2 Alberto Mazzoldi, 3 Danilo De Rossi, 3 Andrew G. Rinzler, 4 Oliver Jaschinski, 5 Siegmar Roth, 5,” *Arch Mech*, vol. 47, p. 859, 1995.
[53] G. M. Spinks, G. G. Wallace, R. H. Baughman, and L. Dai, “Carbon Nanotube Actuators: Synthesis, Properties, and Performance,” *Electroact. Polym. EAP Actuators Artif. Muscles Real. Potential Chall.*, pp. 261–95, 2004.
[54] G. Krishnan, J. Bishop-Moser, C. Kim, and S. Kota, “Kinematics of a generalized class of pneumatic artificial muscles,” *J. Mech. Robot.*, vol. 7, no. 4, p. 041014, 2015.
[55] C. S. Kothera, M. Jangid, J. Sirohi, and N. M. Wereley, “Experimental Characterization and Static Modeling of McKibben Actuators,” *J. Mech. Des.*, vol. 131, no. 9, p. 091010, 2009.
[56] G. K. Klute, J. M. Czerniecki, and B. Hannaford, “McKibben artificial muscles: pneumatic actuators with biomechanical intelligence,” in *Advanced Intelligent Mechatronics, 1999. Proceedings. 1999 IEEE/ASME International Conference on*, 1999, pp. 221–226.
[57] S. A. F and S. C. P, “Apparatus for measuring the hardness of materials,” US1770045 A, 08-Jul-1930.
[58] B. Woods, E. Bubert, C. Kothera, J. Sirohi, and N. Wereley, “Experimental Testing of Pneumatic Artificial Muscles for Trailing Edge Flap Actuation,” 2007.
[59] N. Wereley, C. Kothera, E. Bubert, B. Woods, M. Gentry, and R. Vocke, “Pneumatic Artificial Muscles for Aerospace Applications,” 2009.
[60] E. Bubert, B. Woods, C. Kothera, and N. Wereley, “Design and Fabrication of a Passive 1-D Morphing Aircraft Skin,” 2008.

[61] Y.-L. Park *et al.*, “Design and control of a bio-inspired soft wearable robotic device for ankle–foot rehabilitation,” *Bioinspir. Biomim.*, vol. 9, no. 1, p. 016007, Mar. 2014.
[62] M. Wehner *et al.*, “A lightweight soft exosuit for gait assistance,” in *Robotics and Automation (ICRA), 2013 IEEE International Conference on*, 2013, pp. 3362–3369.
[63] M. Pohl, “A Motion Seat Using Pneumatic Membrane Actuators In A Hexapod System Structure,” in *6th International Workshop on Research and Education in Mechatronics*, Annecy, France, 2005.
[64] J. Radojicic, D. Surdilovic, and G. Schreck, “Modular hybrid robots for safe human-robot interaction,” *World Acad. Sci. Eng. Technol. WCSAT 2009*, 2009.
[65] A. A. Stokes, R. F. Shepherd, S. A. Morin, F. Ilievski, and G. M. Whitesides, “A Hybrid Combining Hard and Soft Robots,” *Soft Robot.*, vol. 1, no. 1, pp. 70–74, Mar. 2014.

6.3 Python Script

```
import smbus
import time
import RPi.GPIO as GPIO

GPIO.setmode(GPIO.BCM)   #Setup GPIO pins 17 and 18 as outputs
GPIO.setwarnings(False)
GPIO.setup(17,GPIO.OUT)
GPIO.setup(18,GPIO.OUT)

desired_pressure=20     #Desired Air Pressure (psi)

pmin=0          #Sensor minimum pressure
pmax=150        #Sensor maximum pressure
outmin=1638     #Output for 10% Calibration
outmax=14746    #Output for 90% Calibration

while 1: #Stopped by user (using CTRL+C) once internal pressure exceeded
80 psi

    GPIO.output(18,GPIO.LOW)
    GPIO.output(17,GPIO.HIGH)

    bus=smbus.SMBus(1)     #Continuously reads air pressure (2 bytes of
data)
    b1=bus.read_i2c_block_data(0x28, 0x88, 2)
    output=((b1[0] & 0x3f)<<8)+b1[1]   #Calculates output from 2 bytes of
data

    pressure= ((output-outmin)*(pmax-pmin)/(outmax-outmin))+pmin
#Calculates Air Pressure

    print ("Pressure : ", pressure, "psi"); #Prints pressure reading

    if pressure >= desired_pressure:
        GPIO.output(17,GPIO.LOW) #Closes valve restricting air flow to
actuator
        time.sleep(10)  #Holds pressure for 10 seconds
        GPIO.output(18,GPIO.HIGH) #Allows actuator to vent air pressure
        time.sleep(5)   #Allows actuator to vent for 5 seconds
        desired_pressure=desired_pressure+10 #Increases desired air
pressure by 10 psi
```